Satellite Products and Services Review Board

Enterprise Algorithm Theoretical Basis Document For VIIRS Land Surface Temperature Production

Compiled by the

SPSRB Common Standards Working Group

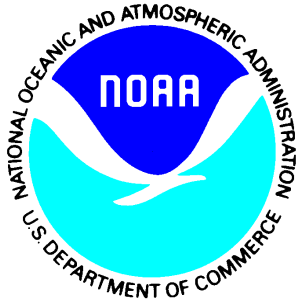

Version 1.3

November, 2021

TITLE: Enterprise Algorithm Theoretical Basis Document for VIIRS Land Surface Temperature Production

AUTHORS:

Yunyue Yu, NOAA/NESDIS/STAR, College Park

Yuling Liu, CICS/UMD, College Park

Peng Yu, CICS/UMD, College Park

Heshun Wang, CICS/UMD, College Park

DOCUMENT HISTORY
DOCUMENT REVISION LOG

The Document Revision Log identifies the series of revisions to this document since the baseline release. Please refer to the above page for version number information.

DOCUMENT TITLE: Algorithm Theoretical Basis Document Template			
DOCUMENT CHANGE HISTORY			
Revision No.	**Date**	**Revision Originator Project Group**	**CCR Approval # and Date**
1.0	Oct. 2017	Developing a new ATBD document	
1.1	Mar. 2018	Updates according to feedback from ARR	
1.2	Apr. 2019	Update the quality flag matrix, snow mask input switch from NWP to snow cover EDR and quality flag bits order	
1.3	Nov. 2021	Update the retrieval error section	

LIST OF CHANGES

Significant alterations made to this document are annotated in the List of Changes table.

DOCUMENT TITLE: Algorithm Theoretical Basis Document Template					
LIST OF CHANGE-AFFECTED PAGES/SECTIONS/APPENDICES					
Version Number	**Date**	**Changed By**	**Page**	**Section**	**Description of Change(s)**
1.1	03/23/2018	Yuling Liu			Updated the validation results analysis; input data description
1.2	04/01/2019	Yuling Liu		2.2	Updated the snow mask input in 2.2.2
				2.4	Updated the LST quality determination matrix, quality flag table and output items
1.3	11/12/2021	Yuling Liu		2.5	Updated the retrieval error section

TABLE OF CONTENTS

LIST OF TABLES AND FIGURES

PAGE

1 INTRODUCTION

The product description, requirements and satellite instrument description are briefly introduced in this section. Section 2 gives an overview of the land surface temperature (LST) retrieval algorithm and operations concept. In detail, it describes the baseline algorithm, its input and output data, the theoretical background, sensitivity analyses and error budget. Some practical considerations are also described, followed by the validation practices. Assumptions and limitations associated with the algorithm is discussed in Section 3. Finally, Section 4 lists the references cited. Though this document is based on the S-NPP VIIRS, it also applies to the VIIRS sensor onboard J-1, J-2 etc. Section 2.3.2 will provide details on how to use this enterprise algorithm in multiple sensors.

1.1 Product Overview

1.1.1 Product Description

Land surface temperature (LST) is one of the most important parameters in the weather and climate system controlling surface heat and water exchange with the atmosphere (Yu et al., 2012). It has been widely used in a variety of fields such as numerical weather prediction models and data assimilation systems (Meng et al., 2009; Bauer et al., 2010; Zheng et al., 2012, Trigo et al., 2015), evapotranspiration evaluation (Sun et al., 2012, Galleguillos et al.,2011), irrigation and hydrological cycle particularly agricultural drought monitoring (Anderson et al., 2011, 2012, Karnieli et al.,2010; Wan et al., 2004), and urban heat island monitoring (Rajasekar and Weng, 2009; Weng et al., 2004; Weng 2009; Voogt and Oke, 2003). In the United States of America, demands of satellite LST data are from a variety of government agencies including the National Oceanic and Atmospheric Administration (NOAA), Department of Agriculture (DOA), Environmental Protection Agency (EPA), Department of the Interior (DOI), Department of Defense (DOD), as well as from universities and research institutes.

Accuracy of the satellite LST measurement is limited by the atmospheric correction, the complexity of surface emission characteristics, and sensor performance. Therefore, the performance of LST algorithms depends on the retrieval conditions. It is worth mentioning that LST performance varies significantly over region, season, day/night, dry/moist etc. conditions according to published worldwide LST validation results (Yu et al., 2009b, 2012; Coll et al., 2005, 2010,2012; Hook et al., 2007; Hulley & Hook, 2011; Guillevic et al., 2012; Wan et al., 2002, 2004,2014; Li S. et al., 2014; Li H. et al., 2014; Liu et al., 2015; Göttsche et al., 2016).

By now satellite LSTs have been routinely produced for over forty years from a variety of polar-orbiting and geostationary satellites. For producing an LST climate data record from those programs, consistency among LST products from different satellite missions are considered for better cross-satellite evaluation and better geographic global validation. A

primary objective of the enterprise LST development is to provide a state-of-the-art LST algorithm that is applicable to multiple sensors and has good quality. The enterprise LST algorithm should be simplicity, robust and applicable to both geostationary orbit (GEO) and Low Earth orbit (LEO) satellite missions. Note that the enterprise LST products are available only for cloud clear, probably clear and probably cloudy pixels; and the LUT is stratified for the following conditions: daytime and nighttime, levels of satellite viewing zenith angles and levels of dry and moist atmospheres. Specifications of the LST product such as resolution, accuracy and refresh rate will be described in the next section.

Currently, surface emissivity variation is still the biggest impediment in satellite LST retrieval. The remote sensing community has been working for years to obtain high quality and time series of global land surface emissivity (LSE) maps (e.g., Borbas et al., 2008; Seemann et al., 2008; Hulley & Hook, 2009; Hulley et al., 2015). The enterprise LST algorithm should potentially benefit from such technical improvement of emissivity estimation. Concurrent with the enterprise LST development, the global gridded emissivity product is also developed to support the emissivity explicit LST algorithms. For details about the emissivity algorithm, please refer to the emissivity ATBD.

1.1.2 Product Requirements

Product requirements were defined in the satellite missions. Table 1-1 provides the LST accuracy and precision requirements for the JPSS mission, which also applies to the requirements for this enterprise VIIRS LST algorithm.

Table 1-1 Product requirements from JPSS L1RD

Accuracy	1.4 K
Precision (1 sigma)	2.5 K
Measurement Range	213 – 343 K
Refresh Rate	At least 90% coverage of the globe every 12 hours
Horizontal Resolution	0.8 km

The enterprise LST product is in Netcdf4 format with associated quality flag and metadata information. The accuracy and precision listed in table 1-1 is only for confidently clear pixels. The LST product has a latency requirement of 96 minutes allocated to Environmental Satellite Processing Center (ESPC) processing. More details about the requirements, please refer to the document for JPSS risk reduction project requirement.

1.2 Satellite Instrument Description

Visible Infrared Radiometer Suite (VIIRS) onboard S-NPP and future JPSS series e.g. J-1, J-2 etc., a scanning radiometer, collects visible and infrared imagery and radiometric measurements of the land, atmosphere, cryosphere, and oceans. VIIRS extends and improves upon a series of measurements initiated by the Advanced Very High-Resolution Radiometer (AVHRR) and the Moderate Resolution Imaging Spectroradiometer (MODIS). VIIRS data is used to measure land surface temperature, as well as cloud and aerosol properties, ocean color, sea surface temperature, ice motion and temperature, fires, and Earth's albedo. Climatologists use VIIRS data to improve our understanding of global climate change.

Table 1-2 VIIRS bands and bandwidths

VIIRS Band	wavelength (μm)	Bandwidth (μm)	NEDT/SNR	Dynamic Ranges (W m^{-2} sr^{-1} μm^{-1})	Spatial resolution (m)
M1	0.412	0.402-0.422	*352,316	*30-135,*135-615	750m
M2	0.445	0.436-0.454	*380,409	*26-127,*127-687	
M3	0.488	0.478-0.488	*416,414	*22-107,*107-702	
M4	0.555	0.545-0.565	*362,315	*12-78,*78-667	
M5(B)	0.672	0.662-0.682	*242,360	*8.6-59,*59-651	
M6	0.746	0.739 - 0.754	199	5.3-41.0	
M7(G)	0.865	0.846 - 0.885	*215,340	*3.4-29,*29-349	
M8	1.240	1.23 - 1.25	74	3.5-164.9	
M9	1.378	1.371 - 1.386	83	0.6-77.1	
M10(R)	1.61	1.58 - 1.64	342	1.2-71.2	
M11	2.25	2.23 - 2.28	10	0.12-31.8	
M12	3.7	3.61 - 3.79	0.396	230-353K	
M13	4.05	3.97 - 4.13	*0.107,0.423	230-634K	
M14	8.55	8.4 - 8.7	0.091 K	190-336K	
M15	10.763	10.26 - 11.26	0.070 K	190-343K	
M16	12.013	11.54 - 12.49	0.072 K	190-340K	
DNB	0.7	0.5 - 0.9		$3e^{-9}$~$2E^{-2}$wcm^{-2}sr^{-1}	750m
I1(B)	0.64	0.6 - 0.68	119	5-718	375m

I2(G)	0.865	0.85 - 0.88	150	10.3-349	
I3(R)	1.61	1.58 - 1.64	6	1.2-72.5	
I4	3.74	3.55 - 3.93	2.500 K	210-353K	
I5	11.45	10.5 - 12.4	1.500 K	190-340K	

Note: *dual gain band, spectral radiance in unit of $wm^{-2}sr^{-1}$ μm^{-1}. Shaded channels are used for LST retrievals.

VIIRS provides global moderate-resolution data twice daily without any gap. It is a scanning radiometer with a total field of regard of 112.56° in the cross-track direction. At a nominal equatorial altitude of 829 km, the swath width is ~3060 km, providing full global daily coverage in both day and night.

As shown in table 1-2, VIIRS has 22 spectral bands covering wavelengths from 0.4 to 12.5 μm, providing data for the production of more than 20 Environmental Data Records (EDRs). Among the 22 bands, there are 16 moderate-resolution bands (M bands, each with 16 detectors) with a spatial resolution of 750 m at nadir, five imaging resolution bands (I bands, each with 32 detectors) with a 375 m spatial resolution at nadir, and one panchromatic DNB with a near constant 750 m spatial resolution throughout the scan. The M bands include 11 reflective solar bands (RSB) and 5 thermal emissive bands (TEB) which includes the two split window channels used for the LST retrieval. The I bands include 3 RSB and 2 TEB (Cao et al., 2013).

To save transmission bandwidth, VIIRS uses a “bow-tie” deletion to remove duplicated pixels in the off-nadir regions where pixels overlap between adjacent scans (Cao et al., 2013). The advanced design of VIIRS will provide users with finer spatial resolution both at nadir and scan edges.

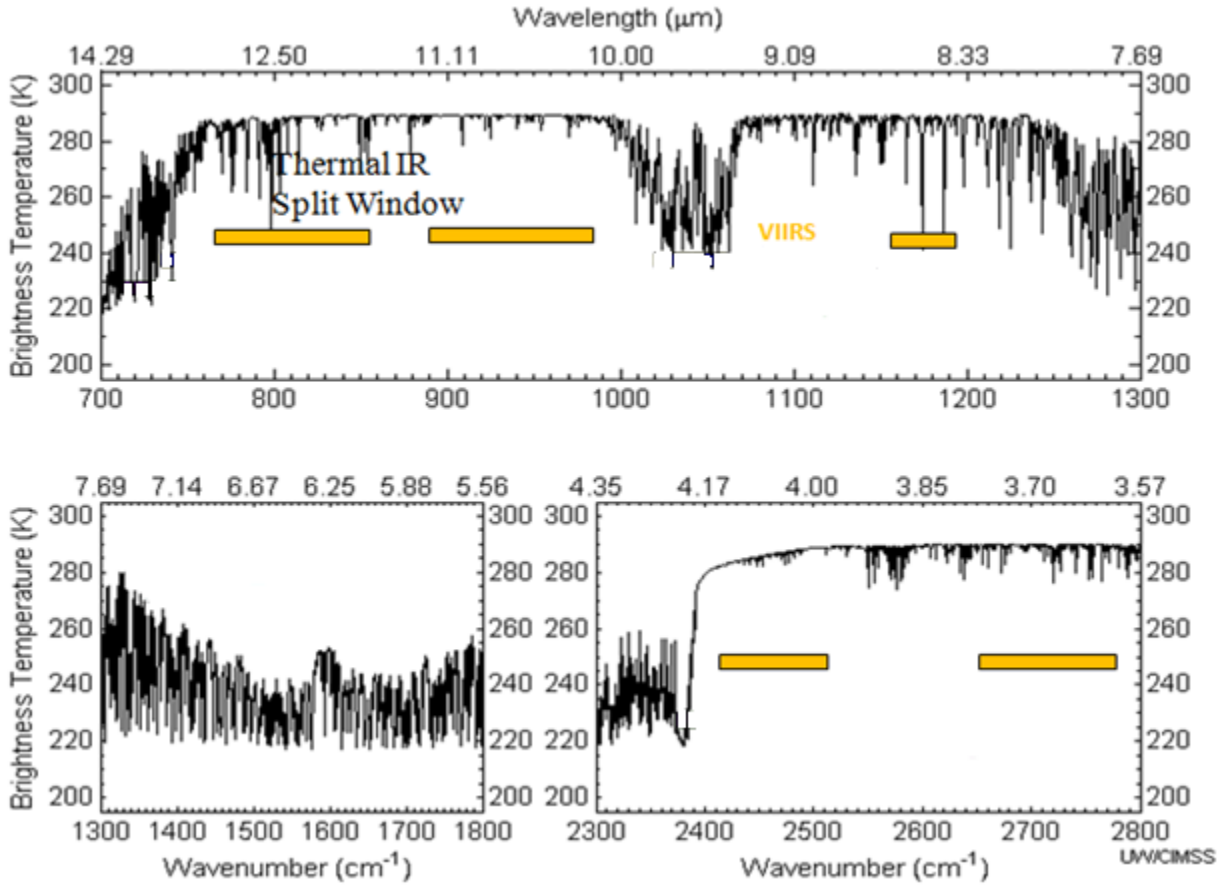

Figure 1-1 Spectral distribution of the VIIRS channels.

The land surface temperature will be produced for each non-confidently-cloudy land pixel observed by the VIIRS sensor. The LST retrieval will rely on data from VIIRS channels M15 and M16 using split window technique.

2 ALGORITHM DESCRIPTION

A generic high-level flowchart of the enterprise LST algorithm is given in the Figure 2-1.

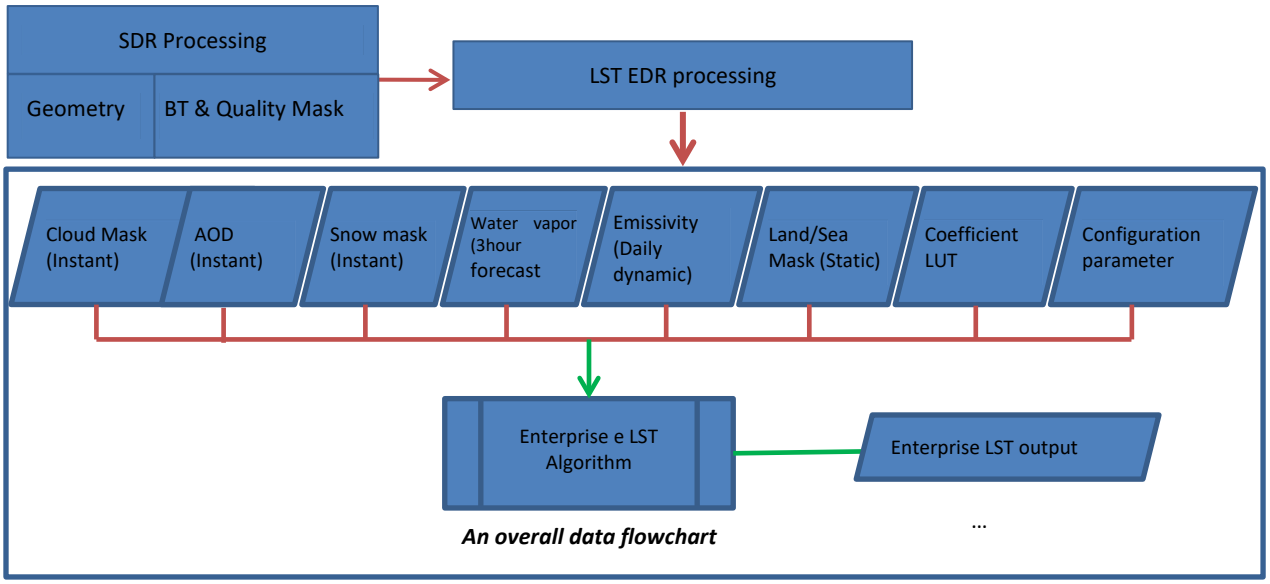

Figure 2-1 High level data flow of the enterprise LST algorithm.

The enterprise LST product is based on a split-window technique that corrects for atmospheric absorption, and applies surface emissivity explicitly in the retrieval. Coefficients of the LST algorithm, which were derived using an atmospheric radiative transfer model (RTM), are stratified by daytime and nighttime conditions, multiple levels of viewing geometry and dry and moist atmospheric conditions. The algorithm is then verified using an RTM simulation dataset and evaluated using S-NPP VIIRS dataset and ground measurements.

2.1 Processing Outline

The processing outline of the LST is summarized in Figure 2-2. It starts from initialization module in which all input and output data are initialized. The pixel level processing checks the non-retrieval conditions as a priority: sea water, bad SDR data, cloudy condition, missing input, BT out of range and emissivity out of range. Any pixel with missing input that includes spectral emissivity, total precipitable water, sensor zenith angle, solar zenith angle, cloud mask and land/sea mask will be skipped for LST retrieval. The valid BT range is set as [190,343] and [190,340] for VIIRS band 15 and band 16, respectively based on the SDR ATBD. The emissivity valid range is set to be [0.8, 1.0] consistent to the settings in the emissivity product. Cloudy condition means that the cloud mask indicates the pixel as

confidently cloudy. If any one of the non-retrieval conditions is met, the LST will be set as a fill value and the corresponding quality flag will be set accordingly. Note that the gridded emissivity product has been developed for this purpose. The nearest neighbor method is used for mapping the gridded emissivity data into granule pixels.

Following that a valid retrieval will be performed. Before calculating LST for each non-confident-cloudy land pixel, day/night time flag is determined from the solar zenith angle (≤ or > 85º) of the sensor geometric data; and dry/moist atmospheric condition flag is determined using the NCEP water vapor information. LST of the pixel is calculated accordingly with the corresponding algorithm coefficients set. Note that LST will be calculated for in-land snow/ice pixels as well and this is indicated in the quality control flags. Large view angle will be flagged also. Finally, the calculated LST values and their associated quality control flags, which were generated in each of the above steps, are combined with the LST product package and are written to files for user access.

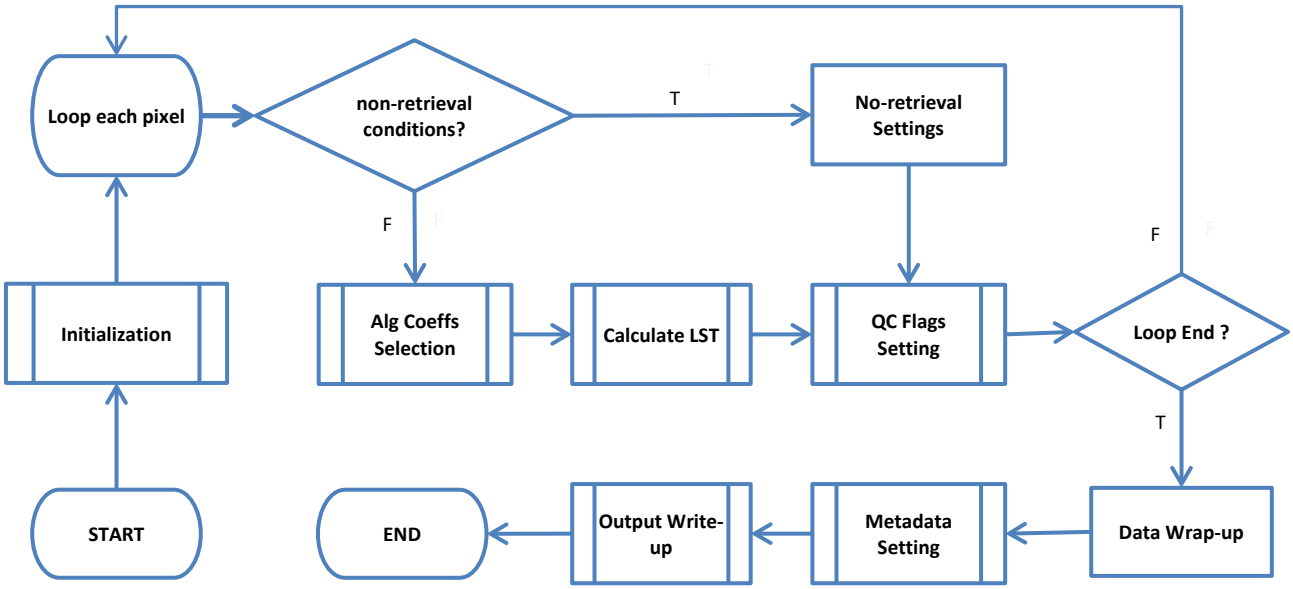

Figure 2-2 High Level Flowchart of the LST production for illustrating the main processing steps.

2.2 Algorithm Input

This section describes the input needed to process the LST product. While the LST is derived for each pixel, ancillary datasets are required as well as the upstream data. Note that some input e.g. cloud mask and AOD for the enterprise LST derivation is from enterprise products.

2.2.1 Primary Sensor Data

The list below contains the primary sensor data used for the LST retrieval. By primary sensor data, we mean information that is derived solely from the sensor observations and geolocation information, or the level 1b data. Table 2-1 lists those input sensor data and their descriptions.

Table 2-1Input list of primary sensor data.

Name	Description	Dimension	Unit
Brightness temperature at 11μm	brightness temperature at 11μm	grid (xsize, ysize)	K
Brightness temperature at 12μm	brightness temperature at 12μm	grid (xsize, ysize)	K
Latitude	Pixel latitude	grid (xsize, ysize)	Degree
Longitude	Pixel longitude	grid (xsize, ysize)	Degree
Solar zenith	solar zenith angles	grid (xsize, ysize)	Degree
View Zenith	Satellite view zenith angle	grid (xsize, ysize)	Degree
SDR QC flags	Level 1b data quality	grid (xsize, ysize)	unitless

SDR channel input:

SDR channel brightness temperatures at 11μm (band M15) and 12μm (band M16) are used for LST calculation directly.

Geolocation data:
Latitude and longitude information for each pixel is needed to map ancillary data to the sensor pixels.

Viewing geometry information:
Solar zenith angle is needed to determine day and night condition. The satellite view zenith angle is used for atmospheric path correction, which is stratified in the algorithm coefficient. Details of their usage for LST derivation will be described in later sections.

Quality flags in the level 1 data:
Any inherent QC flags in the level 1 SDR data will be read and applied before generating LST using the selected algorithm. Any missing/bad pixels will be skipped.

2.2.2 Derived Sensor Data

The derived sensor data sets used for the LST retrieval are listed in Table 2-2 and described in this section.

Table 2-2 Input list of derived sensor data.

Name	Description	Dimension	Unit
Cloud mask	Enterprise cloud mask (ECM) data	grid (xsize, ysize)	unitless
Snow mask	Snow mask from snow cover EDR	grid (xsize, ysize)	unitless
Land/sea mask	NASA land/sea mask data	grid (xsize, ysize)	unitless
water vapor	NCEP tpw data	grid (xsize, ysize)	mm(cm)
Emissivity	Land surface emissivity	grid (xsize, ysize)	unitless
AOD	Enterprise AOD data	grid (xsize, ysize)	unitless

Cloud mask:
The ECM product has been used as input, which provides 4-level cloud scheme indicating four cloudiness conditions for each pixel: clear, probably clear, probably cloudy, and cloudy. It also provides the information for thin cirrus and active fire.

Total precipitable water:
NCEP forecast data is used as the source for TPW input. Its coarse spatial resolution and quality has been a concern for LST performance. Sensitivity test is conducted and introduced in the section of sensitivity analysis. If TPW data is available from the sensor of the same satellite platform, it shall be used as the input.

Surface emissivity:
A set of spectral (i.e., the split-window channels) LSE data is required for this emissivity explicit enterprise LST algorithm An LSE algorithm development is on-going, which provides a global daily LSE product for the LST derivation. This product has a special resolution of 0.009 degree and will be mapped to the resolution of this LST product.

Snow mask:
The enterprise snow cover EDR is used which provides a binary snow mask at I-band spatial resolution of 375 m therefore the data preprocessing is performed for snow mask input by mapping the data from 375 m to 750 m.

Land/sea mask:
The NASA land/sea mask will be used. Several categories are available in the land/sea mask, including shallow, moderate and deep oceans, land, shoreline, shallow, ephemeral, and deep inland water. LST will be calculated for all land and inland water pixels.

AOD (aerosol optical depth):
The enterprise AOD will be used in the determination of AOD related quality flags. Note that the AOD is not retrieved at nighttime when the solar zenith angle is greater than 90 degree (Laszlo and Liu, 2016). If the solar zenith angle of all pixels in a granule are over 90 degree,

there will be no AOD file input. In this case, the AOD flag is set as default value "1". Meanwhile a global metadata will indicate that there is no AOD input for the granule. Therefore, the quality bit of AOD equal to 1 has two meanings: it means AOD out of range when there is valid AOD retrieval, otherwise it should be interpreted as fill value.

2.2.3 Algorithm Coefficients and Control values

In addition to the primary and derived sensor data, algorithm coefficients and the threshold values for selection of the coefficient dimension and for quality control flags are ingested as the input. Table 2-3 lists the file information for the coefficients LUT and its dimension criterion. QC flag criteria and details of the algorithm selection will be given in the following section.

Table 2-3 Input list of coefficient and configuration files

Name	Description	Dimension	Unit
Coefficients	Algorithm coefficient file	2*3*5*7	Unitless
Parameter	Configuration value file		Unitless

The dimension of the coefficient LUT is defined as: 2 represents day/night separation; 3 represents the dry/moist separation which is currently set as three levels: very dry condition (tpw in the range of 0-1.5 cm), dry condition (tpw in the range of 1.5-3.0 cm) and moist condition(tpw greater than 3.0 cm); 5 represents the viewing angle separation which is currently set as 5 levels i.e. 0-25 degree, 25-45 degree, 45-55 degree, 55-65 degree and 65-75 degree; 7 represents the coefficient items of the LST formula. Note that the coefficient LUT structure is flexible. The number of levels and values in each range can be adjusted.

2.3 Theoretical Description

2.3.1 Physical Description

Under clear sky condition, the at-sensor measured radiance within the TIR spectral range (8-14μm) can be described by

$$I(\lambda) = I_s(\lambda) + I_{atm}(\lambda)^{\uparrow} + I_{atm}(\lambda)^{\downarrow} \quad (3.1)$$

where $I_s(\lambda)$, $I_{atm}(\lambda)^{\uparrow}$ and $I_{atm}(\lambda)^{\downarrow}$ represent the radiance contributions from surface emission, atmospheric upwelling and reflected downwelling sky irradiance, respectively; λ is the wavelength of the sensing channel. The radiance components and their relationship are illustrated in figure 2-3.

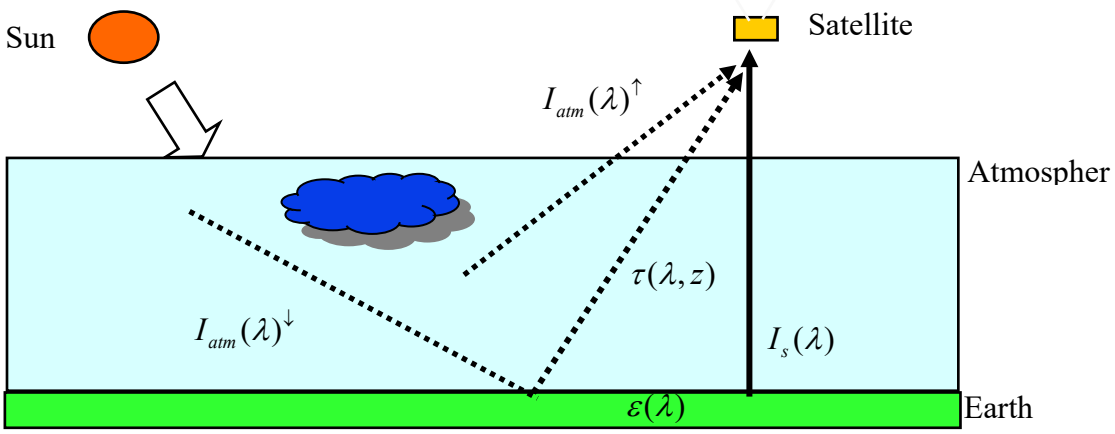

Figure 2-3 Radiation components reached to satellite sensor.

Satellite LST retrievals are usually performed in infrared (IR) bands where the surface emission reaches its maximum, yet atmospheric absorption is significantly small. In TIR bands, each of the components in Eq. (3.1) can be expressed mathematically by,

$$I_s(\lambda) = \varepsilon(\lambda)\tau_0(\lambda)B(\lambda,T_s)$$
$$I_{atm}(\lambda)^{\uparrow} = \int_z^0 B(\lambda,T_p(z))\frac{\partial\tau(\lambda,z)}{\partial z}dz \qquad (3.2)$$
$$I_{atm}(\lambda)^{\downarrow} = (1-\varepsilon(\lambda))\tau_0(\lambda)\int_0^z B(\lambda,T_p(z))\frac{\partial\tau(\lambda,z)}{\partial z}dz$$

where ε is the surface emissivity, τ is the atmospheric transmittance (τ_0 is the atmospheric transmittance from surface), Z is the height from surface, Ts is the surface temperature, Tp (z) is the atmospheric temperature at height z and $B(\lambda,T_s)$is the spectral radiance ($W\cdot m^{-2}\cdot \mu m^{-1}\cdot \mathrm{sr}^{-1}$) emitted by a blackbody at temperature Ts and wavelength λ(μm), which can be calculated using Planck function.

$$B_\lambda(T_s) = \frac{c_1}{\lambda^5(\exp(\frac{c_2}{\lambda T})-1)} \qquad (3.3)$$

where c_1 and c_2 are constants $c_1 = 1.191\cdot 10^8\ \mathrm{W}\cdot\mu m^4\cdot \mathrm{sr}^{-1}\cdot m^{-2}$
$c_2 = 1.439\cdot 10^4\ \mu m\cdot \mathrm{K}$

Eq. (3.1) and (3.2) are the so-called radiative transfer equations. All these magnitudes depend on the observation angle. From Equation (3.2), the earth surface emitted radiance $I_s(\lambda)$ is a function of temperature and emissivity and gets attenuated along the atmospheric path to the sensor. The purpose of the LST algorithm is to retrieve the land surface temperature Ts from the satellite sensor measured radiance$I_s(\lambda)$. In this problem, the surface temperature is physically coupled with two other factors: the surface emissivity and the atmospheric absorptions. Developing an LST algorithm means to find a solution of decoupling the emissivity and the atmospheric absorption effects from the satellite received radiance.

2.3.2 Mathematical Description

An analytic solution to equation (3.1) is not practical, because the integration of the terms requires good knowledge of the atmospheric profiles which is usually not available in real time processing. It is worth noting that all variables in Eqs. (3.1 & 3.2) are channel effective values except for the angles. If the radiance is measured in N channels, there will be always N+1 unknown, i.e. N emissivities in each channel and an unknown LST for N equations, even multiple channels of information are available. To solve this ill-posed problem, many approaches have been proposed (e.g., McMillin, 1975, Walton et al., 1998; Gillespie et al., 1996; Hook et al., 1993; Dash et al.,2002).

2.3.2.1 Candidate algorithms

Over the past several decades, many algorithms have been proposed to treat the characteristics of various sensors onboard different satellites with different assumptions and approximations for the radiative transfer equation and LSEs. These algorithms can be roughly grouped into three categories: single-channel methods, multi-channel methods, and multi-angle methods, provided that the LSEs are known a priori. If the LSEs are not known, then the algorithms can be categorized into three types: stepwise retrieval method, simultaneous retrieval of LSEs and LST with known atmospheric information, and simultaneous retrieval (Li et al., 2013). The most widely used approach is the split window (SW) technique, in which the atmospheric effects are compensated using two or more adjacent TIR channels (typically at 10-12.5μm). The SW approach was first proposed by McMillin (1975) and has been successfully applied to retrieve sea surface temperature (SST). This method is simplistic and computationally efficient and does not require accurate atmospheric profiles. Encouraged by the success of the SW method for SST retrieval from the satellite measurements, many SW approaches have been proposed for LST retrieval (Atitar & Sobrino, 2009; Becker & Li, 1990; Prata 1994; Price, 1984; Tang et al., 2008; Wan & Dozier, 1996, Sun et al., 2004) and widely used for producing the operational LST products (e.g., Prata, 1993 and 1994; Wan, 1999; Caselles et al., 1997; Yu et al., 2009; Sun et al., 2004; Hulley et al., 2012; Baker, 2013; Trigo et al., 2009). However, its application to LST retrieval is challenging due to the following reasons: first, compared to water surface, thermal IR (TIR) emissivity of most land surface types varies considerably from unity, leading to significant errors in the linearization of the radiative transfer equation which forms the basis for the SW technique (McMillin and Crosby, 1984; Yu and Barton, 1994); second, topographical and vegetation structural variability is complicated and satellite sensed brightness temperatures over a given target can differ significantly from pixel to pixel; moreover, spatial heterogeneity is more significant over land than over ocean, and a retrieved LST represents a complex integration of the observed signal within a pixel; finally, the spatial

and temporal variation of atmosphere over land is almost always greater than that over oceans.

The VIIRS LST product for S-NPP satellite currently uses the surface type dependent SW approach, where coefficients are stratified according to the surface type and day/night conditions. Emissivity is not explicitly required in the algorithm. The enterprise LST algorithm will use emissivity explicitly as the input with the term of $(T_{11}-T_{12})^2$ being exclude because:

1) The S-NPP LST algorithm performance presents a strong dependency on the accuracy of the surface type input.
2) The emissivity variability cannot be well characterized by the surface type particularly those with considerate seasonal or annual change. In addition, the surface type is in general mixed and heterogeneous at the moderate pixel footprint (e.g. 1 km) which results in the mis-representation of the actual emissivities at different error levels.
3) The $(T_{11}-T_{12})^2$ term may lead to large LST uncertainty under specific conditions, e.g., when significant BT difference between the two split window bands (this can be as high as 16K over Australia) occurs. The simulation database is not sufficient to cover such situations.

We studied various SW LST algorithms from the literature (Price, 1984; Ulivieri and Cannizaro, 1985; Becker and Li, 1990; Prata and Platt, 1991; Vodal, 1991; Ulivieri *et al*., 1992; Sobrino *et al*., 1993; Sobrino *et al*., 1994; Wan and Dozier, 1996; Caselles *et al*., 1997; Coll *et al*., 1997; Yu *et al*., 2008), and adapted seven (Table 2-4) as candidate algorithms for enterprise LST production. This is based on the comprehensive study for GOES-R ABI LST algorithm. Yu *et al*. (2008) showed that, if an algorithm's coefficients are determined for typical column water vapor amounts, algorithm accuracy can degrade significantly at large view angles unless a corrective term is applied. Therefore, in this study, five candidate algorithms are with explicit path length correction term, i.e. $(T_{11}-T_{12})(\sec\theta-1)$, in the equation and the other two used stratified coefficients for different viewing angle ranges. Algorithm 1, 3, 4, 5 and 6 are composed of two parts: the base split window algorithm and path length correction, while algorithm 2 and 7 uses implicit path correction by stratifying the retrieval with different satellite viewing angles.

Table 2-4 Candidate LST retrieval Algorithms

No	Formula#	Reference
1	$T_s = C + (A_1 + A_2\frac{1-\varepsilon}{\varepsilon} + A_3\frac{\Delta\varepsilon}{\varepsilon^2})(T_{11}+T_{12})$ $+(A_4 + A_5\frac{1-\varepsilon}{\varepsilon} + A_6\frac{\Delta\varepsilon}{\varepsilon^2})(T_{11}-T_{12}) + D(T_{11}-T_{12})(\sec\theta$	Adapted Wan & Dozier (1996); Becker & Li (1990).
2	$T_s = C + (A_1 + A_2\frac{1-\varepsilon}{\varepsilon} + A_3\frac{\Delta\varepsilon}{\varepsilon^2})(T_{11}+T_{12}) + (A_4$ $+ A_5\frac{1-\varepsilon}{\varepsilon} + A_6\frac{\Delta\varepsilon}{\varepsilon^2})(T_{11}-T_{12})$	Wan & Dozier (1996); Becker & Li (1990).

3	$T_s = C + A_1 T_{11} + A_2(T_{11} - T_{12}) + A_3\varepsilon + D(T_{11} - T_{12})(sec\,\theta - 1)$	Ulivieri & Cannizzaro (1985). (ABI)
4	$T_s = C + A_1 T_{11} + A_2(T_{11} - T_{12}) + A_3(T_{11} - T_{12})\varepsilon_{11} + A_4 T_{12}\Delta\varepsilon + D(T_{11} - T_{12})(sec\,\theta - 1)$	Price(1984)
5	$T_s = C + A_1 T_{11} + A_2(T_{11} - T_{12}) + A_3(1 - \varepsilon_{11}) + A_4\Delta\varepsilon + D(T_{11} - T_{12})(sec\,\theta - 1)$	Coll & Valor (1997).
6	$T_s = C + A_1 T_{11} + A_2(T_{11} - T_{12}) + A_3\varepsilon + A_4\varepsilon(T_{11} - T_{12}) + A_5\Delta\varepsilon + D(T_{11} - T_{12})(sec\,\theta - 1)$	Adapted Enterprise Alg.
7	$T_s = C + A_1 T_{11} + A_2(T_{11} - T_{12}) + A_3\varepsilon + A_4\varepsilon(T_{11} - T_{12}) + A_5\Delta\varepsilon$	Enterprise algorithm

#Note:
T_{11} and T_{12} represent the top-of-atmosphere brightness temperatures at ~11μm and 12 μm, respectively;
$\varepsilon=(\varepsilon_{11}+\varepsilon_{12})/2$ and $\Delta\varepsilon=(\varepsilon_{11}-\varepsilon_{12})$, where ε_{11} and ε_{12} are the spectral emissivity values of the land surface at ~11μm and 12 μm channels, respectively;
θ is the satellite view zenith angle.
C, A_1, A_2, A_3, A_4, A_5, A_5 and D are algorithm coefficients.
Alg 2 and 7 are carried out in different satellite view zenith angle ranges, *i.e.*, [0, 25, 45, 55, 65, 75]

As with most SW algorithms, the candidate algorithms explicitly use LSE values, which can accommodate within class variability (Yu *et al.*, 2005). And it allows easy incorporation of the new and improved global emissivity products (e.g. Hulley & Hook, 2009; Hulley et al., 2015).

2.3.2.2 Algorithm selection

To select a suitable algorithm for the enterprise LST production, we analyzed the theoretical accuracy and sensitivity of the candidate SW algorithms using a comprehensive simulation dataset. It is found that all candidate algorithms give similar accuracy with slightly different uncertainty. The accuracy/precision of the candidate algorithms were evaluated using ground LST data from the SURFace RADiation (SURFRAD) network, Baseline Surface Radiation Network (BRSN) and Global Radiation Group (GMD), and using proxy data from multiple sensors. The algorithm 7 was selected as the enterprise algorithm because of its consistent good performance over multiple sensors, simplicity and robustness.

The MODTRAN atmospheric radiative transfer model (Berk et al., 2000) has been widely used in satellite remote sensing studies for over three decades. We used the MODTRAN 5.2 in this study, which uses an improved molecular band model, termed the Spectrally Enhanced Resolution MODTRAN (SERTRAN). It has a much finer spectroscopy (0.1 cm^{-1}) than its predecessors (1 cm^{-1}), resulting in more accurate modeling of band absorption features in the longwave TIR window regions (Berk et al. 2005). The radiative transfer simulation procedure is illustrated in Figure 2-4.

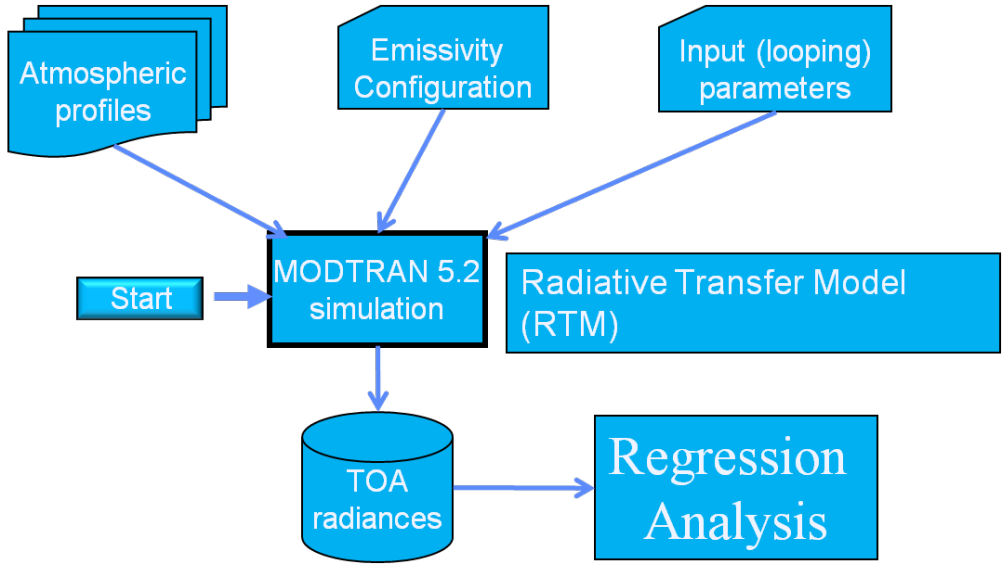

Figure 2-4 Radiative transfer simulation procedure.

The atmospheric profile database consists of 126 profiles generated from cloud-free radiosonde data available from the CrIS F98-Weather Products Test Bed Data Package (NOAA88, Rev. 1.0) and 354 profiles from Thermodynamic Initial Guess Retrieval (TIGR). TIGR data set, in its latest version, is a climatological library of 2311 representative atmospheric situations selected with statistical methods from 80,000 radiosonde reports (Chédin et al., 1985; Claud et al., 1991; Chevallier et al., 1998). Each situation is described, from the surface to the top of the atmosphere, by the values of the temperature, water vapor and ozone concentrations on a given pressure grid. TIGR profiles were checked by means of a cloud test in order to exclude impacts from cloud (Galve, 2008). The profiles represented a variety of atmospheric conditions, spanning a column water vapor range from 0.2 to 7.5 g/cm^2 and a surface air temperature range from 240 to 306 K (Figure 2-5) and spanned from 60º South to 70º North in latitude.

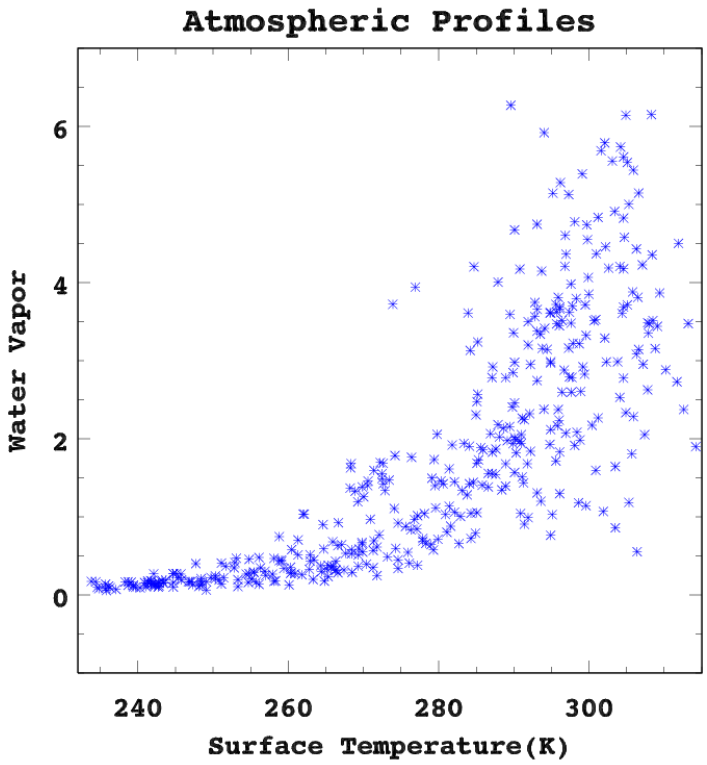

Figure 2-5 Distributions of total column water and surface air temperatures of the atmospheric profiles used in the simulation analyses.

To simulate a wide range of environmental conditions using a limited profile set, we followed Yu *et al.* (2005) and varied the prescribed LST for each profile in a range as $Ts - 10 < LST < Ts + 10$ *K*, where *Ts* is the surface temperature of the profile, with a *1 K* increment. For each prescribed LST, we iterated the prescribed sensor view zenith angle from 0 to 70º with 10º increment and emissivity from 0.90 to 0.999 with a step of 0.00125.

2.3.2.3 Regression analysis

Upon simulating the top-of-atmosphere radiances, we then conducted regression analyses for the algorithm development. The regression procedure is illustrated in Figure 2-6.

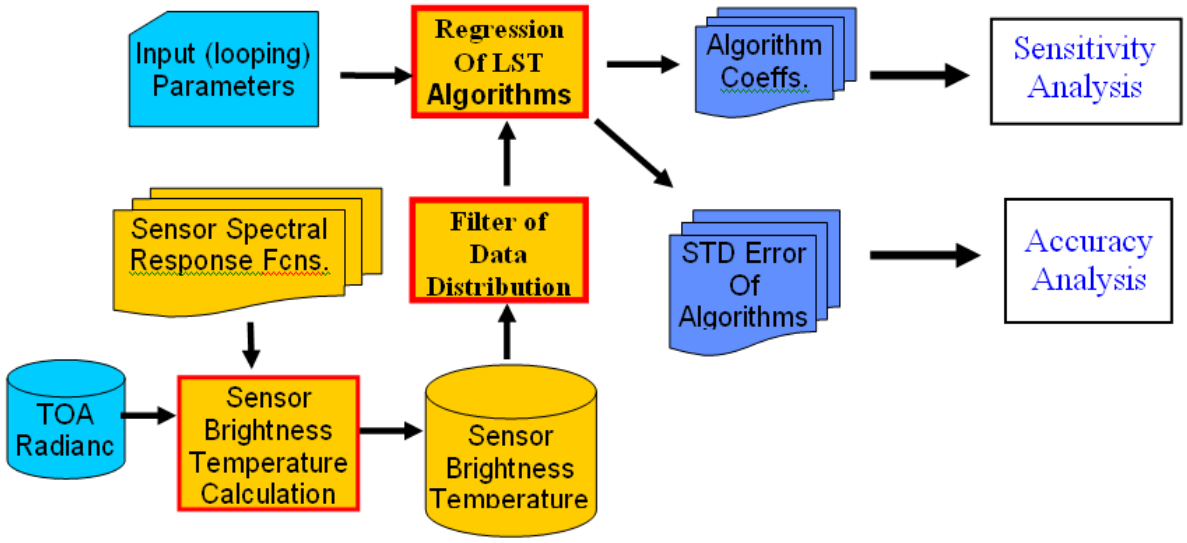

Figure 2-6 Procedure of the algorithm regression analyses.

We first determined the mean channel radiance by integrating over the sensor spectral response function (SRF). The channel radiances were converted into corresponding brightness temperatures using the Planck function. This step constructs the sensor brightness temperature database for regression of the LST algorithms. For another sensor with different SRF, e.g., VIIRS on J-1 or J-2, the above step will be repeated.

Because water vapor is the most significant atmospheric absorber in the thermal bands, we stratified the simulation data according to the water vapor content: 1) “very dry” atmosphere, where the total column water vapor is less than 1.5 g/cm^2, 2) “dry” atmosphere, where the total column water vapor is between 1.5 and 3 g/cm^2, 3)“moist” atmosphere, where the water vapor content is between 3 and 4.5 g/cm^2 and 4)“very moist” atmosphere, where the water vapor content is greater than 4.5 g/cm^2 . It is acknowledged that warmer atmosphere has larger capacity of water vapor, which degrades the LST retrieval.

Due to significant differences in the discontinuity between LST and air temperature, during daytime and nighttime, many LST retrieval algorithms (or accompanying coefficient sets) were specified uniquely for daytime or nighttime use. Daytime and nighttime profiles were separated in the regression. In addition, to better simulate real satellite data, we added Gaussian-distributed random noise to both the simulated brightness temperatures and the surface emissivity values. The standard deviations of the sensor Noise Equivalent Delta Temperature (NEΔT) and the surface emissivity noise are 0.1 K and 0.015 (unitless), respectively.

Before conducting regression analysis with the simulated data and candidate algorithms, we also considered the natural Gaussian-like distribution of land surface and surface air temperatures as noted in Justin *et al.* (NGST technical report, personal communication, 2006). Figure 2-7 shows the filtering results for the daytime dataset. A similar process was applied to the nighttime dataset.

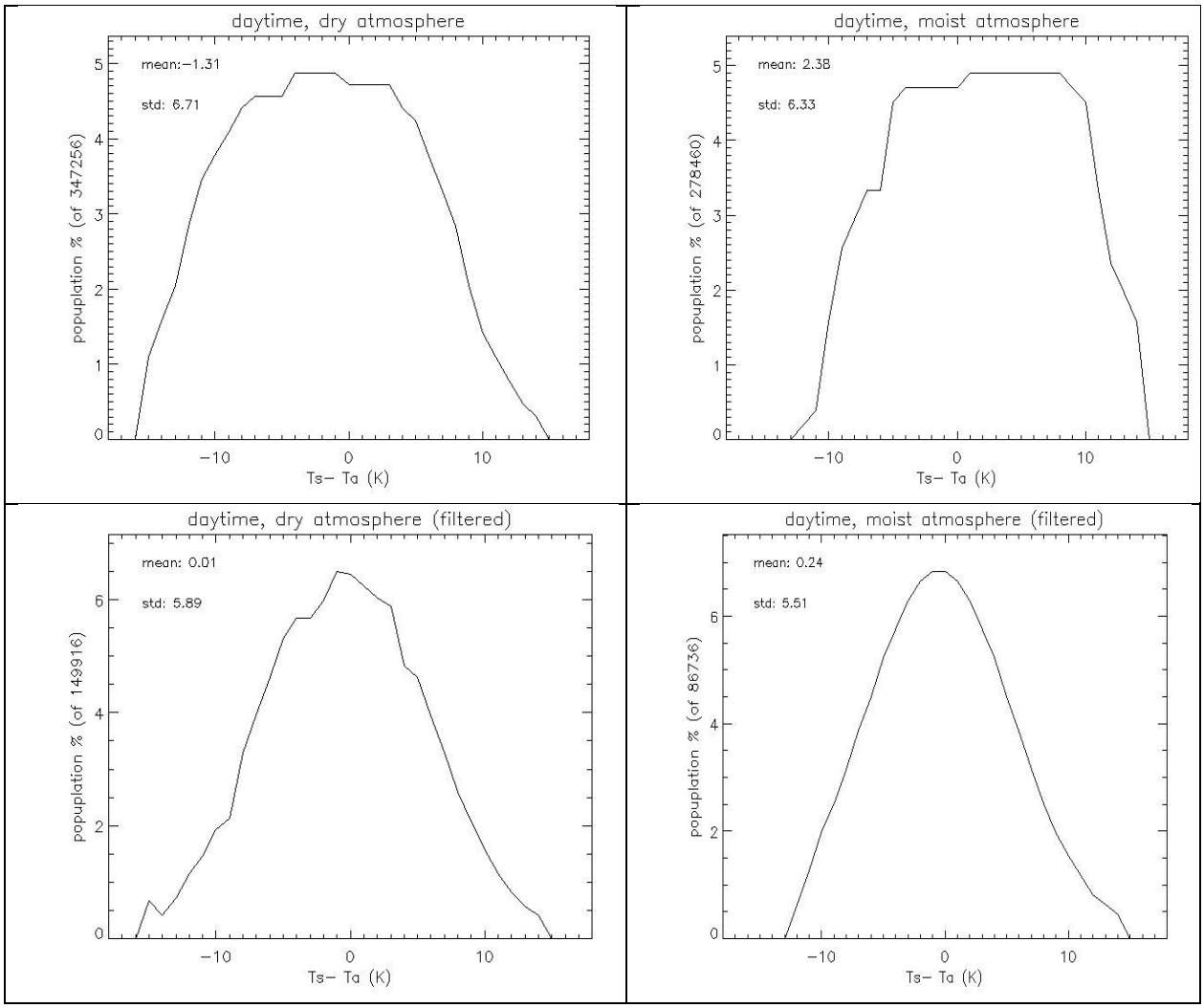

Figure 2-7 Daytime simulation data distribution in terms of the land surface and surface air temperature differences. The original simulation data (top panels) are pretty much evenly distributed in range of the temperature differences. The filtered data for both the dry (left) and moist (right) atmospheres are shown in the bottom panel.

2.4 Algorithm Output

The algorithm output includes LST values, associated quality flags as well as the related emissivity values including the spectral emissivity of the two split window channels, broadband emissivity and associated emissivity quality flags. To minimize the file size, the LST value is stored as a scaled value in 16-bit integer type. The emissivity value is stored as scaled value in 8-bit integer type. Scale factor and offset as well as valid range, fill value etc. are provide as the data attributes. The quality flags are 2-byte bitwise short integer, which contains quality information of LST production for each pixel. The LST values and quality flags data arrays are described in Table 2-5. In the meantime, upon user request, the viewing geometry including satellite zenith angle and azimuth angle is added into the LST output.

Table 2-5 Algorithm output data.

Name	Description	Data Type	Dimension	Unit
LST values	Retrieved land surface temperature value for each pixel. Scaling factor is 0.005, offset is 200, corresponding to Eq (3.7). Therefore, the valid retrieval range is from 2600 to 28600 corresponding to the range of 213K to 343K.	Short	grid (xsize, ysize)	K
LST quality flags	Bit-based quality control flags for each pixel	Short	grid(xsize, ysize)	unitless
Emissivity at 11 micron	Retrieved land surface emissivity value at 11μm for each pixel.	Byte	grid (xsize, ysize)	unitless
Emissivity at 12 micron	Retrieved land surface emissivity value at 12μm for each pixel	Byte	grid (xsize, ysize)	unitless
Broadband Emissivity	Retrieved broadband land surface emissivity value for each pixel	Byte	grid (xsize, ysize)	unitless
LSE quality flags	LSE quality control flags for each pixel	Byte	grid (xsize, ysize)	unitless

The 2-byte LST quality flag indicates SDR quality, atmospheric condition, emissivity source, surface cover, and LST quality. Its definition is provided in Tables 2-6.
Overall LST pixel quality is represented by the quality bit field. Pixel quality is flagged as “No Retrieval” and the corresponding LST will be filled: (Bad SDR) or (missing input) or (Land/Water Flag is “SeaWater”) or (Cloud Confidence is “Confidently Cloudy”) or (BT out of range) or (spectral emissivity out of valid range) or LST < 0 (determined after attempt is made to retrieve LST).

Table 2-6 Product quality information flags

bit	Flag	Source	description
1-0	LST quality	LST	00=high, 01=medium, 10=low, 11=no retrieval
3-2	Cloud condition	Cloud mask	00=confidently clear, 01=probably clear,10=probably cloudy,11=confidently cloudy
4	SDR quality	SDR	0=normal, 1=bad data (bad quality or missing or out of space)
5	Aerosol Optical Thickness at 550 nm (slant path)	AOD	0=within range (AOD<=1.0);1=outside range (AOD >1 or AOD missing)
7-6	Land surface cover	land/sea mask snow/ice mask	00=land;01=snow/ice;10=in land water;11=coastal
9-8	Water vapor condition	Tpw input	00=very dry atmosphere(wv<1.5g/cm^2) ; 01= dry [1.5,3); 10=moist atmosphere[3,4.5); 11= very moist[4.5+)
10	Emissivity quality	Emissivity	0=within LSE uncertainty, 1=beyond LSE uncertainty requirement (0.015)
11	Degradation by large viewing angle	SDR	0=no degradation, 1=large view degradation (VIIRS: <=40 degree)
12	Day/night flag	SDR	0=night (solar zenith angle > 85degree), 1=day
13	Thin cirrus	Cloud Mask	0= no thin cirrus, 1= thin cirrus (Only available for daytime)
14	Fire contamination flag	Cloud mask	0= no, 1= yes
15	Reserved		Reserved for future use

Figure 2-8 illustrates how quality flags are set. The quality flag is set with sequence: it started from the SDR related quality flag including day/night and degradation by large view angle, followed by the atmospheric condition indicators including dry/moist, AOD, thin cirrus and active fire. The latter two are from the enterprise cloud mask. For the fire algorithm ECM uses the EUMETSAT current operational algorithm as described by Joro et al. The thin cirrus detection works only during the day time. It is found that the snow cover EDR does not have snow information for nighttime, cloudy condition etc., which results that the permanent snow area is flagged as land in the LST quality flag. Therefore, the permanent snow in emissivity data quality flag is used to update the surface cover in the LST quality flag (bits 6-7) for non-ocean pixels.

In addition to the pixel level LST values, and quality control flags, metadata are provided in the LST product describing the product in detail as shown in Table 2-7. The Table 2.8 described the logic for LST quality bits settings.

Table 2-7 Metadata defined for the LST product file.

Metadata List Name	description	Criteria descriptions
minLST	minimum LST value within LST range	LST not fill and LST within range [213,343]
maxLST	maximum LST value within LST range	LST not fill and LST within range [213,343]
meanLST	Mean LST value within LST range	LST not fill and LST within range [213,343]
stddevLST	Standard deviation of LST within LST range	LST not fill and LST within range [213,343]
Percentage_Pixels_inValid	Percentage of invalid pixels	LST < 213 or LST > 343 and LST is not fill
Percentage_Pixels_high_quality	Percentage of high-quality retrievals	LST quality is high (LST is not fill included)
Percentage_Pixels_medium_quality	Percentage of medium quality retrievals	LST quality is medium (LST is not fill included)
Percentage_Pixels_low_quality	Percentage of low-quality retrievals	LST quality is low (LST is not fill included)
Percentage_Pixels_retrieved	Percentage of pixels with LST retrieval	LST is not fill
Percentage_Pixels_largeAngle	Percentage of pixels with large view angle	pixels when stz > 40(VIIRS) and LST is not fill
Percentage_Pixels_land	Percentage of land pixels	land pixels when LST is not fill
Percentage_Pixels_clear	Percentage of pixels under confidently clear or probably clear	pixels when LST is not fill and cloud is marked as confidently clear or probably clear

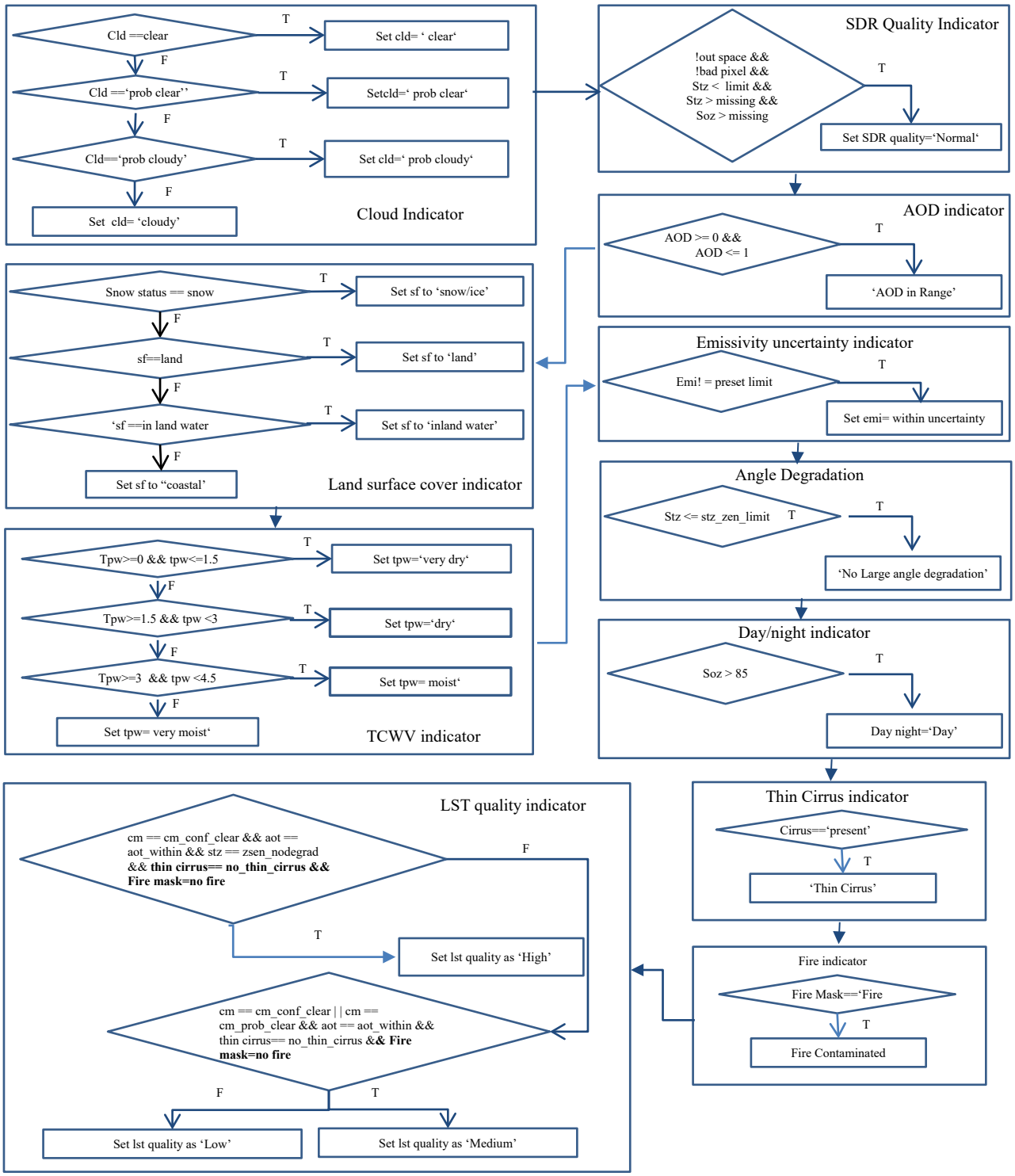

Figure 2-8 Flow chart for quality flag settings

Table 2-8 LST QF/Quality Bit Field Logic Table (Retrieval Cases Only)

LST >= 0	Degraded – Sensor Zenith Angle	Active Fire	AOD Range (AOD available)	Thin Cirrus(day time)	Cloud Confidence Indicator		
					Confident Clear	Probably Clear	Probably Cloudy
T	x	x	x	yes	Low	Low	Low
T	x	x	out	x	Low	Low	Low
T	x	fire	x	x	Low	Low	Low
T	out	no	in	no	Medium	Medium	Low
T	in	no	in	no	High	Medium	Low
F	x	x	x	x	No Retrieval	No Retrieval	No Retrieval

LST >= 0: T = True; F = False
Degraded – Sensor Zenith > 40: out = Outside Range, in = Within Range
Active Fire: no = no active fire; fire = active fire
AOD Range: out = Outside Range, in = Within Range
Thin Cirrus: yes = Thin Cirrus, no = No Thin Cirrus
x = "Indifferent"

Note that AOD is not retrieved under some conditions e.g. nighttime, snow/ice surface, cloud etc. If there is no AOD retrieval, the AOD range criteria will be excluded in above matrix. Similarly, because thin cirrus detection is only available at daytime, it is excluded in above matrix for nighttime pixel LST quality determination.

2.5 Performance Estimates

For each of the 7 algorithms, we calculated the bias and standard deviation (STD) of the regressions. Figure 2-9 shows scatter plots of the regression results for the daytime dry atmosphere cases. It indicates that all algorithms perform well for an LST range from about 220 K to 320 K. The STD of the differences between the prescribed LSTs and the retrieved LSTs ranged from 0.33 K (algorithms 1, 2, 3, 5, 6, 7) to 0.55 K (algorithms 4). It is significantly higher under the moist atmosphere cases, where the value ranged from 0.81 K (algorithm 5) to 0.86 K (algorithm 4). For algorithms 2 and 7, the STD is further stratified with sensor viewing zenith angles. The STD is from 0.35 K to 0.46 K under very dry condition, 0.56 K to 1.06 K under dry condition and 0.65 K to 1.74 K under moist condition for algorithm 7. Algorithm 2 yields similar STD values. The results show a dramatic increase of the regression STD under moist and large viewing angle conditions. For the nighttime cases, similar regression accuracies are observed. STDs of the algorithms under different atmospheric conditions are listed in Table 2-9.

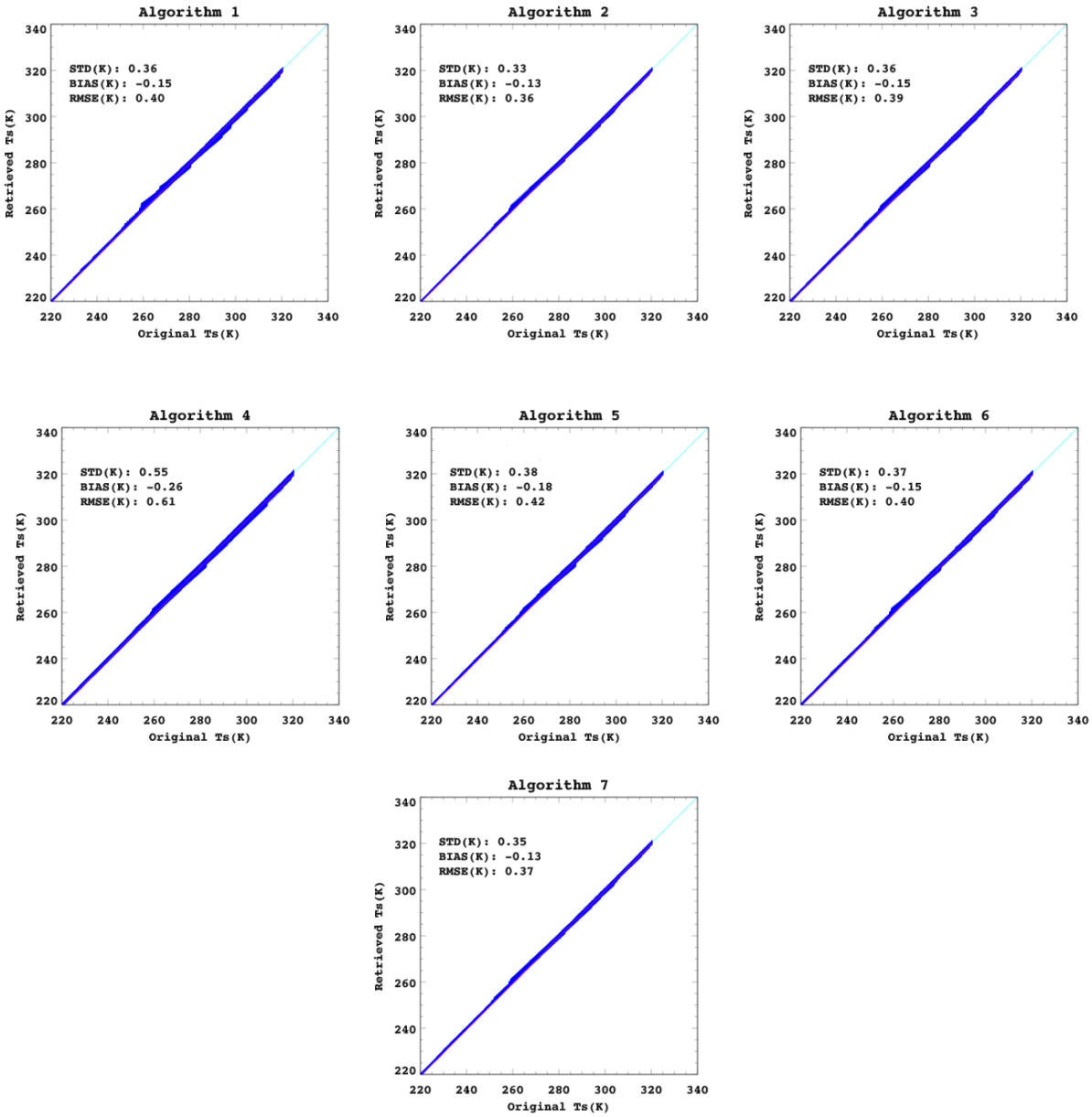

Figure 2-9 Scatter plots of the regression results for the dry atmosphere. Standard deviation (STD) errors of the regression are given in each plot (Daytime).

Table 2-9 Standard deviation errors (K) of the regression analysis.

No	Daytime			Nighttime		
	0-1.5	1.5-3	3-4.5	0-1.5	1.5-3	3-4.5
1	0.36	0.63	0.83	0.34	0.61	0.82
3	0.36	0.62	0.83	0.34	0.61	0.83

4	0.55		0.67		0.86	0.54		0.66		0.85
5	0.38		0.64		0.81	0.36		0.63		0.82
6	0.37		0.63		0.83	0.35		0.61		0.83
2	TPW:0-1.5					TPW:0-1.5				
	0-25	25-45	45-55	55-65	65-75	0-25	25-45	45-55	55-65	65-75
	0.33	0.35	0.36	0.41	0.44	0.31	0.33	0.36	0.40	0.44
	TPW:1.5-3.0					TPW:1.5-3.0				
	0.54	0.58	0.66	0.79	1.09	0.53	0.57	0.64	0.72	0.94
	TPW:3.0-4.5					TPW:3.0-4.5				
	0.63	0.72	0.89	1.12	1.74	0.64	0.71	0.84	1.14	1.66
7	TPW:0-1.5					TPW:0-1.5				
	0.35	0.36	0.38	0.43	0.46	0.32	0.34	0.37	0.42	0.46
	TPW:1.5-3.0					TPW:1.5-3.0				
	0.56	0.6	0.67	0.79	1.06	0.56	0.60	0.65	0.75	0.95
	TPW:3.0-4.5					TPW:3.0-4.5				
	0.65	0.73	0.87	1.12	1.74	0.67	0.74	0.88	1.06	1.67

To have a closer look at error distributions, we produced histogram plots of the regression fits in Figures 2-10 to 2-12 and Figures 2-13 to 2-15 for daytime and nighttime results, respectively. Figures 11-16 reveal that there is no significant bias in any of the algorithms, and the error distributions are fairly symmetric (Gaussian-distribution-like) around 0.15.

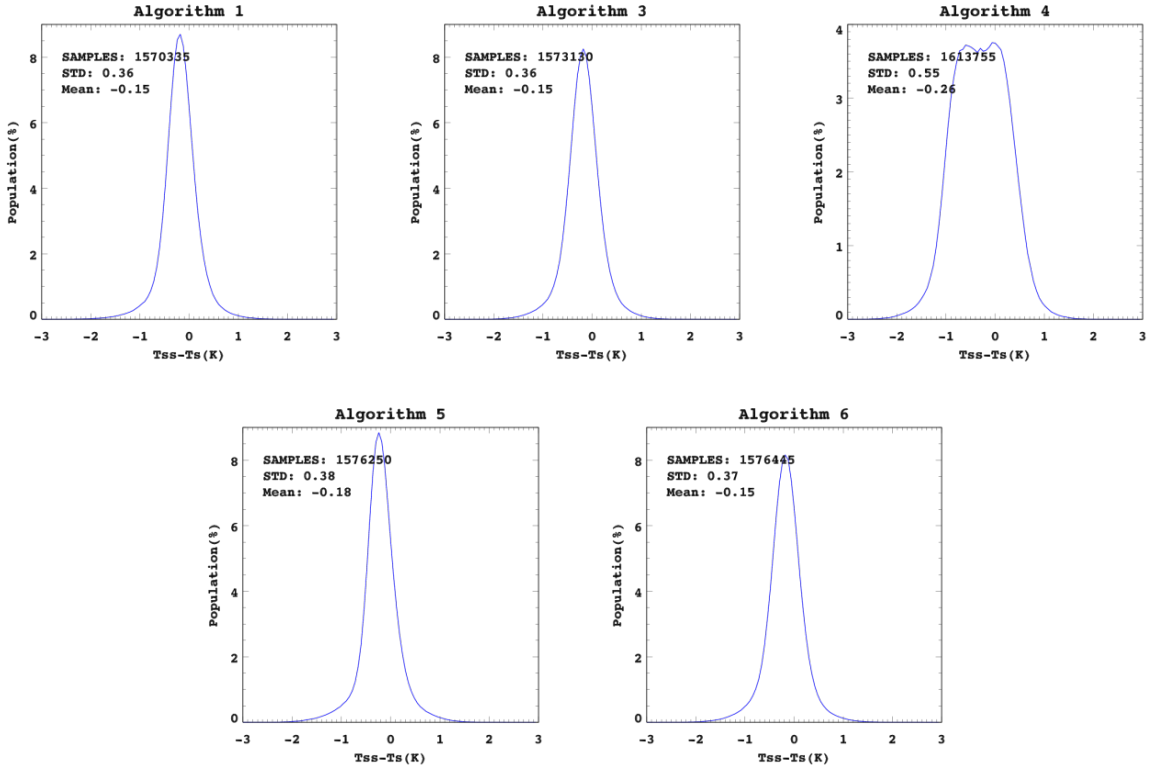

Figure 2-10 Histogram plots of the regression results for the dry atmosphere (tpw: 0.0-1.5 at Daytime). Standard deviation (STD) and mean errors of the regression are given in each plot.

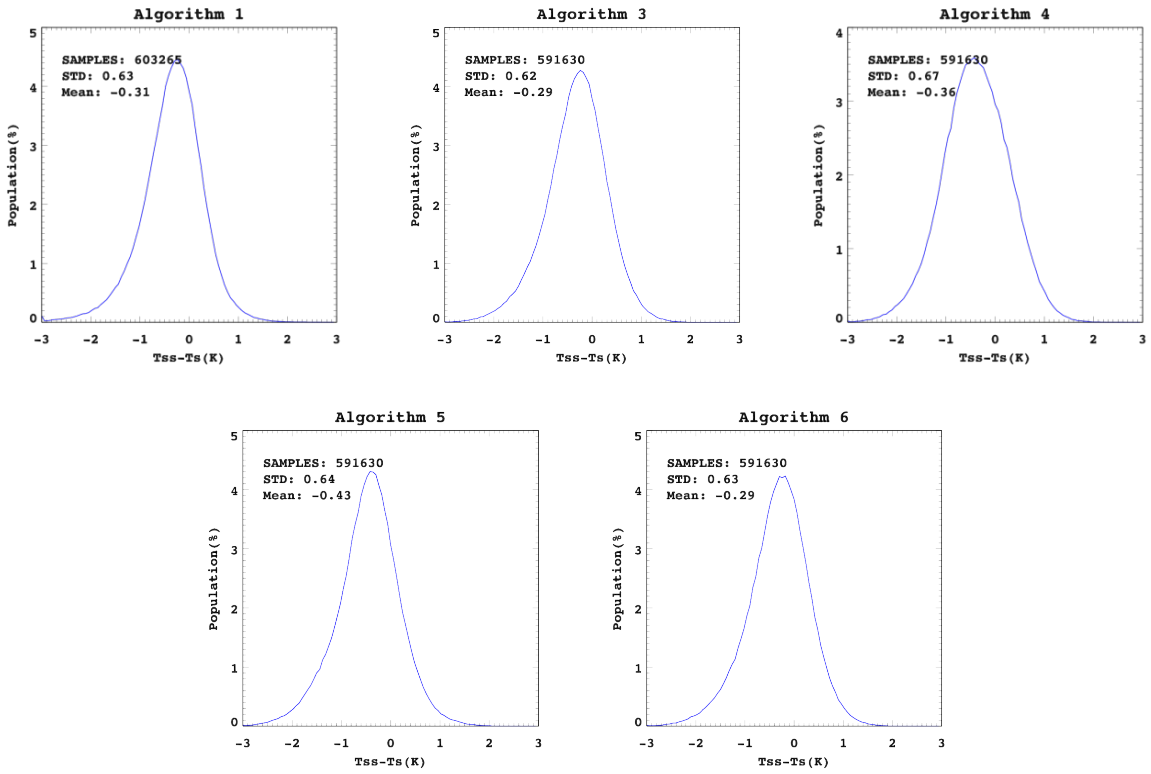

Figure 2-11 Histogram plots of the regression results for the moist atmosphere (Tpw: 1.5-3 at Daytime). Standard deviation (STD) and mean errors of the regression are given in each plot.

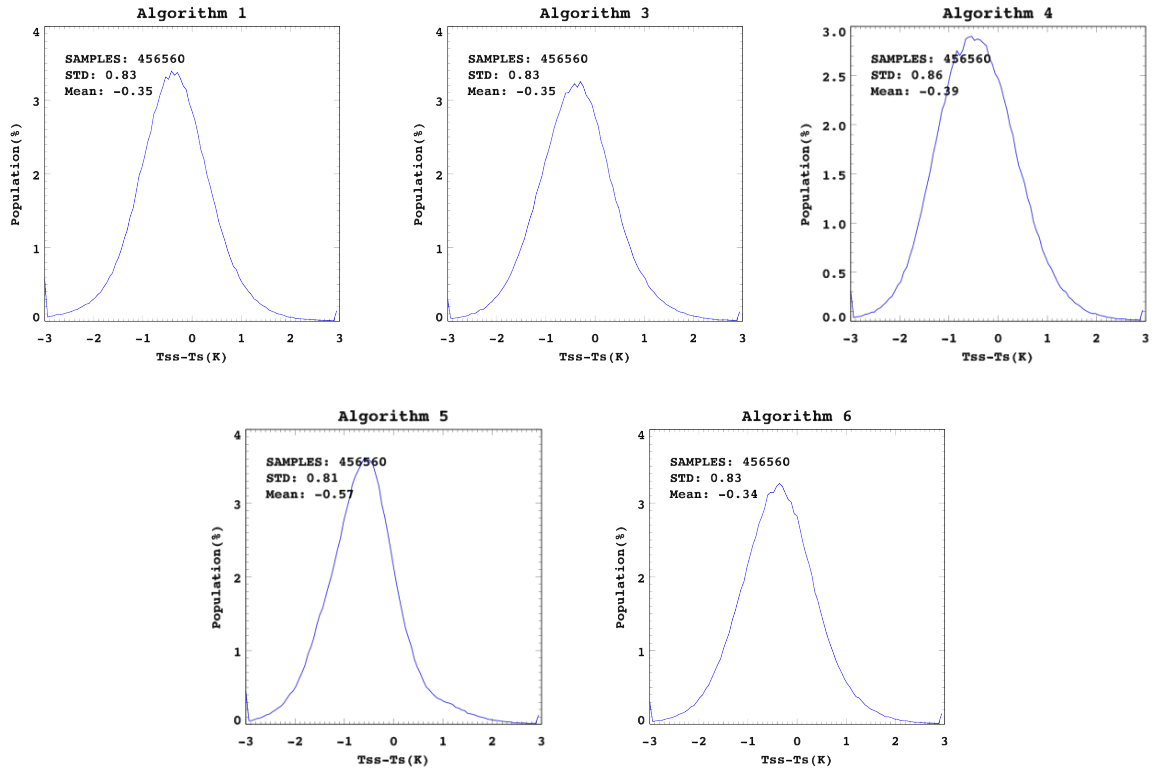

Figure 2-12 Histogram plots of the regression results for the moist atmosphere (Tpw: 3-4.5 at Daytime). Standard deviation (STD) and mean errors of the regression are given in each plot.

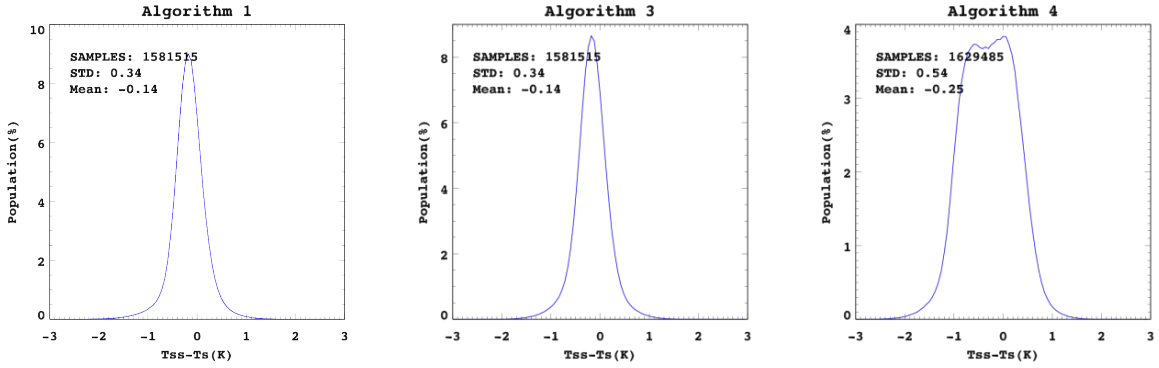

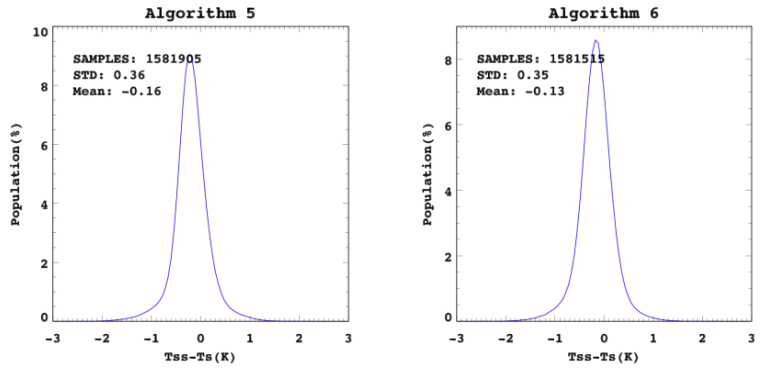

Figure 2-13 Histogram plots of the regression results for the dry atmosphere (Tpw: 0.0-1.5 at Nighttime). Standard deviation (STD) and mean errors of the regression are given in each plot.

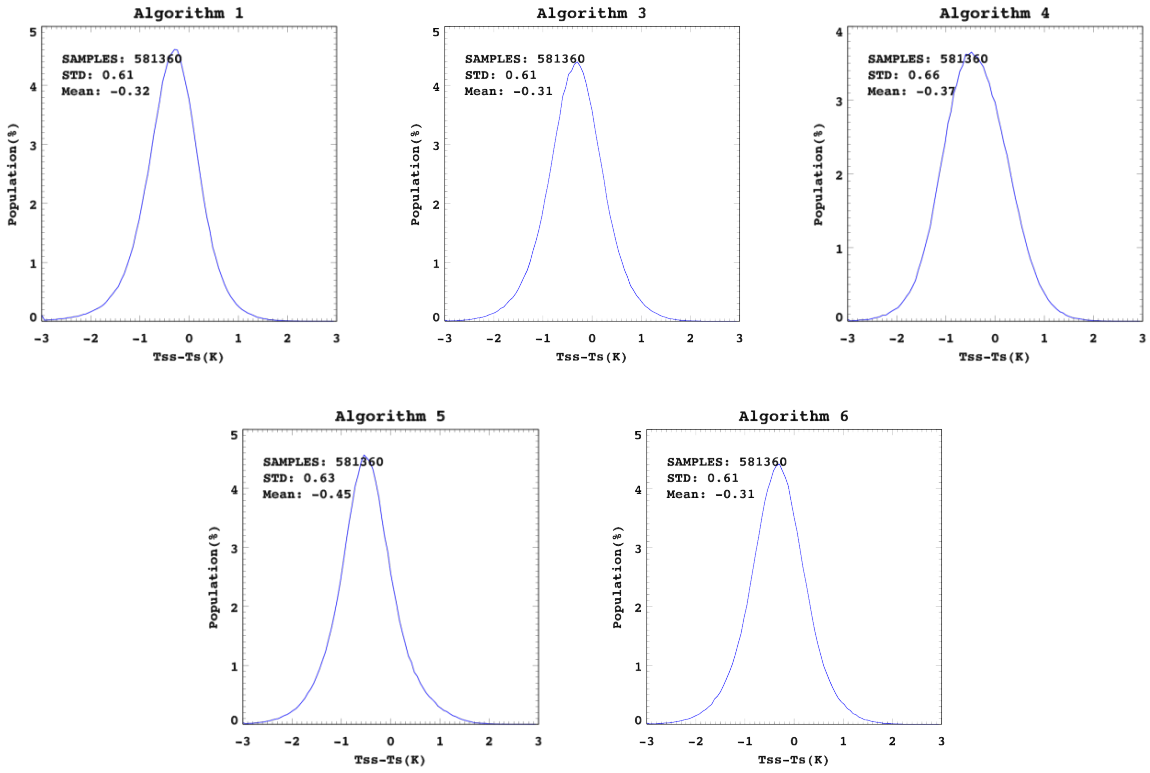

Figure 2-14 Histogram plots of the regression results for the moist atmosphere (Tpw: 1.5-3.0 at Nighttime). Standard deviation (STD) and mean errors of the regression are given in each plot.

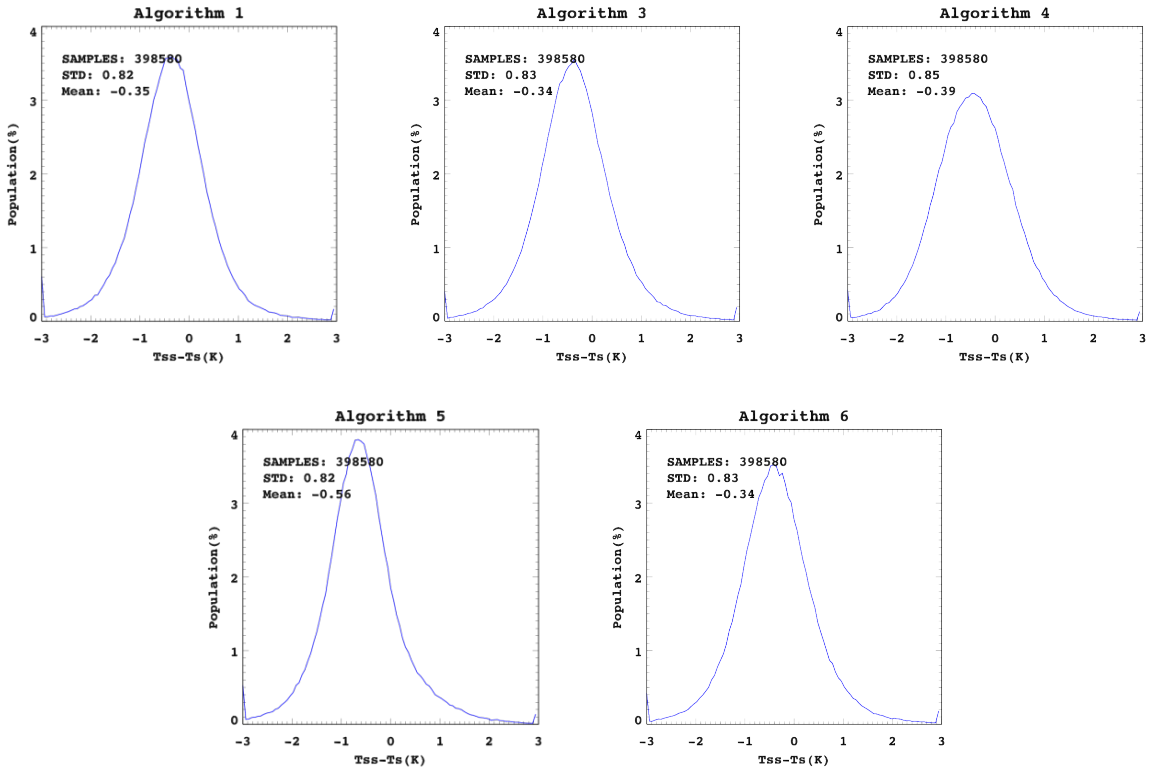

Figure 2-15 Histogram plots of the regression results for the moist atmosphere (Tpw: 3-4.5 at Nighttime). Standard deviation (STD) and mean errors of the regression are given in each plot.

Compared to the daytime algorithm performance, the standard deviation of the nighttime case is slightly better for each algorithm. And the algorithm precision gets worse with increasing water vapor contents and viewing angles.

2.5.1 Test Data Description

As described in Section 2.3.2, the profile collection is composed of 126 profiles generated from radiosonde data and 354 profiles from TIGR. Following the method described in Figure 2-9, the comprehensive simulation database is built up for VIIRS sensor onboard S-NPP satellite. The database depicts the relationships among land surface temperature, sensor brightness temperature, viewing angle, emissivity and TPW etc. This database serves as the test base for theoretical estimation of the enterprise LST algorithm performance. The dataset used for validation is described in section 2.7.

2.5.2 Sensor Effects

The enterprise LST utilizes brightness temperature from VIIRS bands 15 and16 and is affected by the sensor performance including but not limited to the stability of the spectral response function, the sensor noise ratio and accuracy of the radiometric calibration, geolocation error and spectral error. The effects of sensor noise on LST is described in section 2.5.3.1. Geo-location uncertainties for M-bands are ~ 70 m at nadir, meeting specifications at nadir and edge-of-scan (Cao et al., 2013).

2.5.3 Retrieval Errors

Theoretically all inputs may introduce uncertainty to the final LST product. In this study, four important error sources are considered: sensor noise, the surface emissivity uncertainty, the forecast total precipitable water vapor error, and the model error. We therefore analyzed the uncertainty of the candidate LST algorithms (Table 2-4) with respect to the four factors. The simulation dataset described above is used in the following estimations. In the following sections, we only listed the results of the variation and uncertainty estimation for the selected enterprise algorithm.
The overall LST uncertainty is estimated as

$$S_{lst} = \sqrt{S_{sensor}^2 + S_{lse}^2 + S_{tpw}^2 + S_{model}^2} \quad (3.4)$$

Where S_{lst} indicates the overall LST uncertainty; S_{sensor} represents the LST uncertainty attributed to the sensor noise; S_{lse} is the contribution from the LSE uncertainty; S_{tpw} represents the LST uncertainty due to the error of forecast water vapor, and S_{model} is the model error attributed to the regression process. Each error source is assumed mutually independent. The similar method has been used to quantify the uncertainty for SEVIRI LST (Freitas et al., 2010).

2.5.3.1 Sensor noise Uncertainty

Radiometric accuracy is critical for EDR retrieval. The LST uncertainty S_{sensor} due to the sensor noise can be described as,

$$S_{sensor} = \sqrt{\delta T_{m15}{}^2 + \delta T_{m16}{}^2} \quad (3.5)$$

where δT_{m15} and δT_{m16} represent the LST error attributed to the impact of brightness temperature noise at M15 and M16 bands, respectively assuming that the two error sources are uncorrelated. Using algorithm 7 (Table 2-4) as an example, these two components are

$$\delta T_{m15} = (C_1 + C_2 + C_4 * \varepsilon)\delta BT_{11} \quad \text{and} \quad \delta T_{m16} = (-C_2 - C_4 * \varepsilon)\delta BT_{12} \quad (3.6)$$

Therefore, the LST uncertainty with respect to BT uncertainties is

$$S_{sensor} = \sqrt{((C_1 + C_2 + C_4 * \varepsilon)\delta BT_{11})^2 + ((-C_2 - C_4 * \varepsilon)\delta BT_{12})^2} \quad (3.7)$$

The requirement for noise equivalent ΔT (NEdT) is 0.070 and 0.072 (VIIRS SDR ATBD) for the two split window channels onboard VIIRS, therefore δBT_{11} is set to 0.070 and δBT_{12} is set to 0.072 in this study.

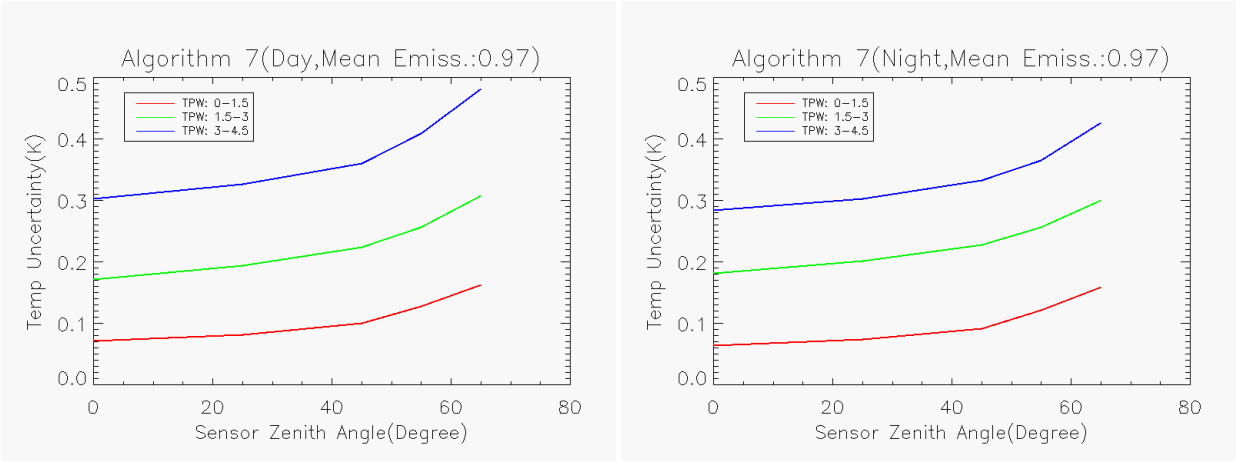

Figure 2-16 LST uncertainty attributed to the sensor noise at three TPW categories under day (left) and night (right) conditions for algorithm 7 assuming the mean emissivity of 0.97, emissivity difference of 0.005 at difference viewing geometries

Figure 2-16 shows the LST uncertainty attributed to the sensor noise for daytime and nighttime conditions. The results indicate that the sensor noise of 0.07 and 0.072 for BT_{11} and BT_{12} may cause LST uncertainty of 0.27 K and 0.25 K for daytime and nighttime, respectively. And the uncertainty increases with water vapor and sensor viewing angles.

2.5.3.2 Emissivity Uncertainty

Analytically, the LST uncertainty S_{lse} due to the emissivity uncertainty can be described as,

$$S_{lse} = \sqrt{S\varepsilon_{11}^2 + S\varepsilon_{12}^2} \quad (3.8)$$

where $S\varepsilon_{11}$ and $S\varepsilon_{12}$ represent the LST uncertainties resulting from the uncertainties of the spectral emissivity at 11 μm and 12 μm, respectively assuming that the two error sources are uncorrelated. Using algorithm 7 (Table 2-4) as an example, these two components are

$$S\varepsilon_{11} = (C_3/2.0 + C_4/2.0 * (T_{11} - T_{12}) + C_5)\delta\varepsilon_{11} \quad (3.9)$$
$$S\varepsilon_{12} = (C_3/2.0 + C_4/2.0 * (T_{11} - T_{12}) - C_5)\delta\varepsilon_{12}$$

Where $\delta\varepsilon_{11}$ and $\delta\varepsilon_{12}$ are the uncertainty of spectral emissivity at 11 μm and 12 μm, respectively. The enterprise LST algorithm uses the NOAA land surface emissivity product as input, which provides the spectral emissivity value and associated uncertainty. The LSE retrieval error budget contains three types of uncertainty sources: the bare ground emissivity uncertainty, GVF error and VCM method uncertainty, snow fraction error and linear mixing uncertainty. The details were described in the LSE ATBD. The mean emissivity errors of the two split window channels are grouped into four bins: [0, 0.005], [0.005, 0.010], [0.010, 0.015] and 0.015 beyond. Taking the LSE of April 9th in 2017 as an example, the above four groups account for 1.17%, 75.91%, 22.88% and 0.04% of the global distributions, respectively. It indicates that the LSE uncertainty is mostly less than 0.01. Since the individual spectral emissivity uncertainty is not available in the current LSE product, the mean value of each bin range i.e. 0.0025, 0.0075, 0.0125 and 0.02 (for bin with emissivity uncertainty greater than 0.015) is used to represent the spectral emissivity uncertainty, assuming the emissivity uncertainties in each band are the same, regardless of day and night. Figure 2-17 shows the global distribution of LSE uncertainty on day Oct. 1st, 2019. The global data with 5 km spatial resolution obtained from long term monitoring system is used in the test. The LST uncertainty attributed to the LSE uncertainty is estimated using equation (3.8) and the result is presented in the right panel of Figure 2-17.

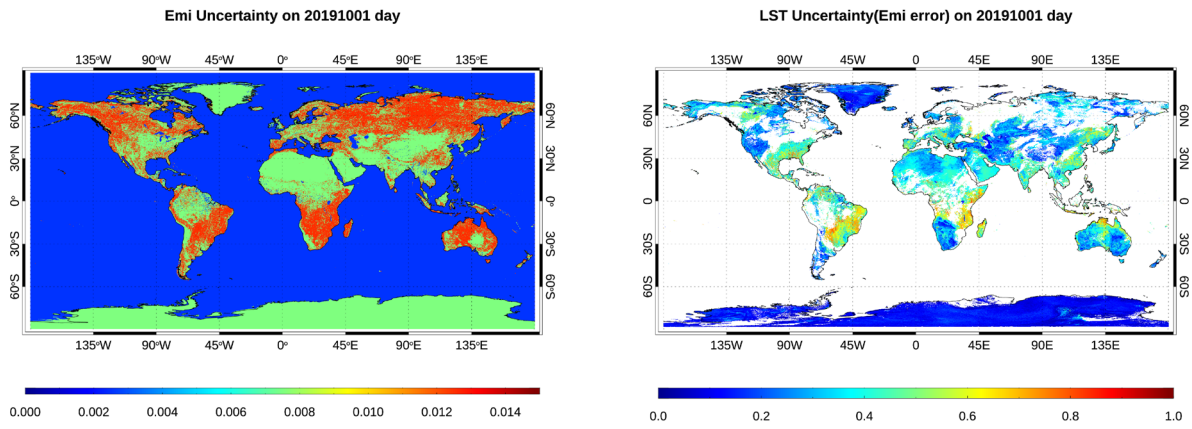

Figure 2-17 Land surface emissivity uncertainty global distribution(left) and its contribution to the LST uncertainty (right) on day Oct. 1st, 2019

S_{lse} is generally below 1 K as shown in Figure 2-187. From the LSE uncertainty map, snow ice surface and barren soil surface has relatively small uncertainty less than 0.008, which caused smaller LST uncertainty.

Similar results were observed for the nighttime cases. Note that the predicted LST uncertainty calculated using equation (3.8) assumes the same LSE uncertainty for both channels, and for both daytime and nighttime. In reality, however, the LSE uncertainty at 12

microns might be larger than that at 11 micron due to the less overlap with ASTER spectral coverage at TIR domain which spans up to 11.65 μm.

2.5.3.3 Water Vapor Uncertainty

Stratifying our regressions by water vapor regime, we assume that water vapor content can be well estimated a priori. In practice, water vapor information is usually available from satellite soundings, ground radiosondes and/or operational numerical weather prediction model forecasts. Two errors may occur. First, the water vapor value may be mis-measured due to a variety of error sources. Second, due to spatial resolution differences between VIIRS data and water vapor data, the TPW in a finer pixel size (e.g. 1 km) might not be well represented by the integrated water vapor measurements over a large area (e.g. 0.25 degree grid). TPW is used indirectly in the enterprise LST algorithm, i.e. LST LUT stratified by the TPW value. The uncertainty in TPW may lead to a wrong LUT used for LST calculation. For example, the coefficient set of the LST algorithm for dry atmospheres may be incorrectly applied to a moist atmospheric condition, and vice-verse. The equation (3.10) is used to calculate the LST uncertainty attributed to the TPW error.

$$S_{tpw}{}^2 = \sum_k \left(LST_j - \widehat{LST_j} \right)^2 P(\widehat{W_J} \,|W) \Big) \qquad (3.10)$$

Where
LST_j is the LST value calculated with class W
$\widehat{LST_j}$ is the LST value calculated with class $\widehat{W}$
P denotes the probability that Wj belongs to the water vapor content class $\widehat{W}$ given the true class of W.

The enterprise LST algorithm makes use of forecast of total water vapor provided by the NCEP GFS for parameter selections. Prior to 2020, the TPW with a spatial resolution of 0.5 degree was used in the operational LST retrieval, and then replaced by data with a finer spatial resolution of 0.25 degree. To characterize the TPW error, we compared the GFS forecast with the NCEP reanalysis data and observations from ARM network and radiosonde data.

ARM provides in-situ precipitable water vapor measurements either instantaneous or hourly mean from microwave radiometer. *Cadeddu et al.* [2013] summarize microwave radiometry uncertainties as due to (i) uncertainties in the measurement of the brightness temperature, (ii) uncertainties in the mean radiating temperature of the modeled atmosphere, (iii) uncertainties in the methodology to retrieve precipitable water vapor from sky brightness temperature, and (iv) uncertainties associated with the radiative transfer model used. All these different uncertainties are taken into account carefully by ARM, providing an approximate total uncertainty of 5% (*Cadeddu et al.*, 2013). Four permanent sites including NSA_C1, SGP_C1, SGP_E39 and SGP_41 were selected considering the temporal overlap

with the forecast TPW at the spatial resolution of 0.25 degree. The ground observation was quality screened with problematic and suspicious data removed. Spatially closest pixel data and temporally linear interpolated GFS TPW was compared with ground observation at specific time. Overall statistics indicates the close agreement between the GFS forecast precipitable water vapor and ARM observations with bias close to 0.05 cm and RMSE less than 0.34. Outliers were observed from the comparison results with higher TPW from the ground observations, which suggests the existence of possibly undetected suspicious observations.

The forecast TPW with forecast hour at 06z,12z and 18z, was compared with respective analysis, for the 15th of each month in 2017 and 2018. The comparison result is shown in the right panel of Figure 2-18.

The radiosonde data collected from 19 sites over CONUS in 2016 was also used to quantify the forecast TPW uncertainty. The comparison result is shown in the middle panel of Figure2-18. Overall it yields nearly zero bias between radiosonde TPW and forecast TPW. Reale et al. (2012) showed the statistics of the NCEP GFS 6-h forecast water vapor compared with in situ measurements based on the NOAA Products Validation System (NPROVS). The BIAS of the water vapor fraction profile is within ±20% of the absolute value below 400 hPa.

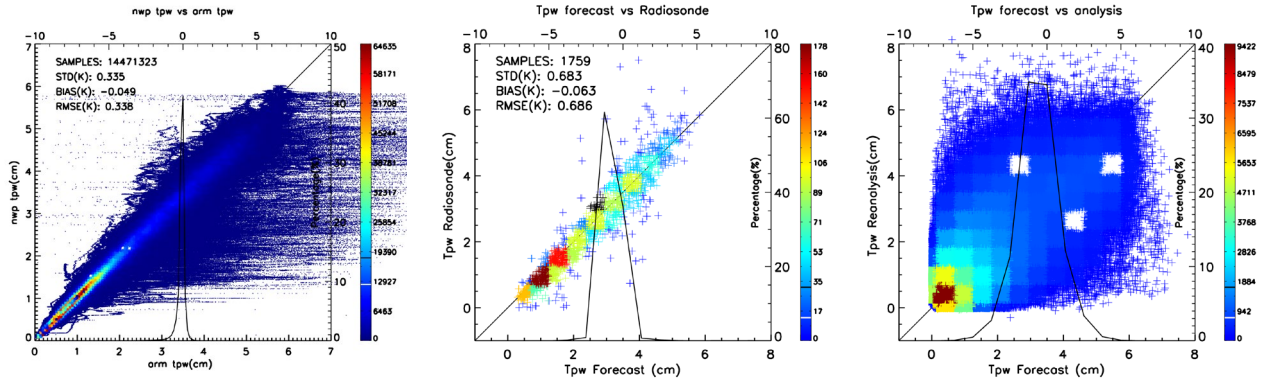

Figure 19 Forecast TPW error against observations from ARM(left), radiosonde(middle) and NCEP reanalysis(right)

The TPW misclassification probability as shown in Figure 2-19 is obtained based on the above combined error analysis. Histogram is calculated for the reference TPW at bin size equal to the TPW interval used in the LUT i.e. 0.5 cm. Those falling into the category of 4.5 cm and over, will be combined so as the total value is used to present the probability for the moistest category.

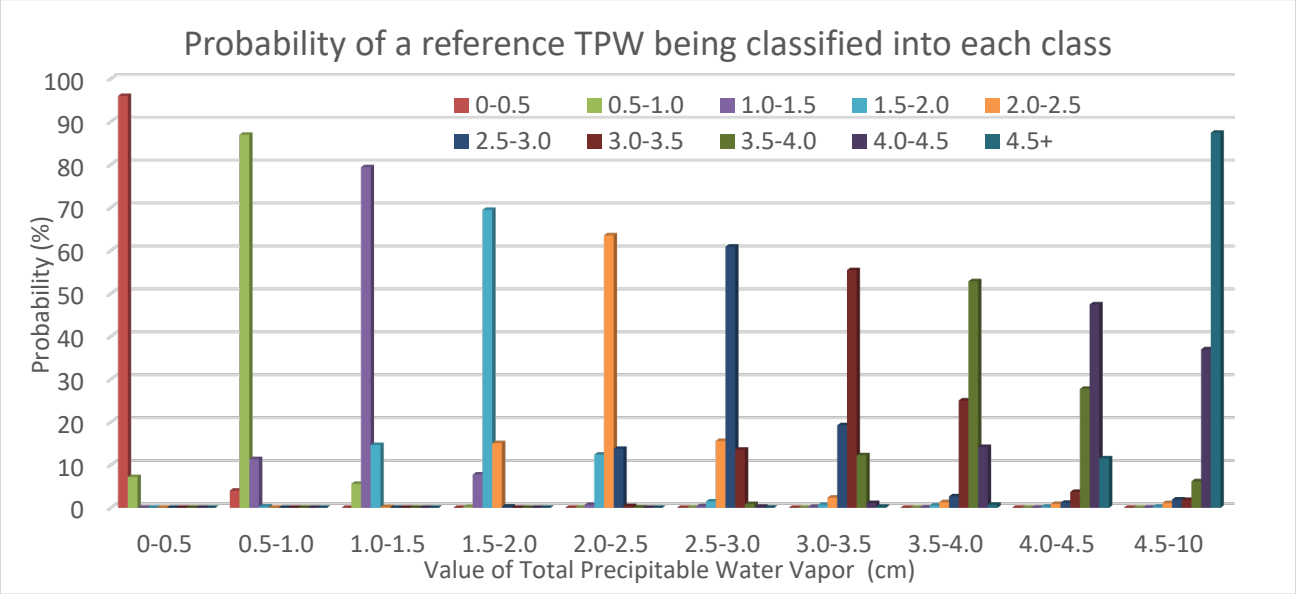

Figure 20 Probability (y axis) of a reference TPW value (x axis) being classified into each TPW class distinguished by color in the legend.

2.5.3.4 Model error

The model error comes from the algorithm regression process, which was discussed in Section 2.3. The root mean square error of the LST regression is used as an indicator of the model error for each class denoted by the combination of day/night, satellite zenith angle and total precipitable water vapor contents. Figure 2-20 presents the model error with finer stratification of TPW and view zenith angle. The model error is generally within ranges between 0.3K to 3K. It tends to increase with the TPW and VZA. It indicates that, for the moist atmospheric conditions, the model error gets worse when the zenith angle is larger than 40 degrees. Similar trends were observed for the nighttime case. For dry atmospheric conditions, the increase trend grows slowly with the angles and the accuracy of the retrieval under dry atmospheric conditions is significantly better than that under moist atmospheric conditions. Similar results were observed by Yu *et al.* (2008). The RMSE is below 2 K for water vapor contents less than 4 cm for all angles, beyond that the model error increases substantially with angles. We note that all algorithms listed in Table 2-4 give similar model error, which primarily indicates the accuracy limitation of the current SW technique.

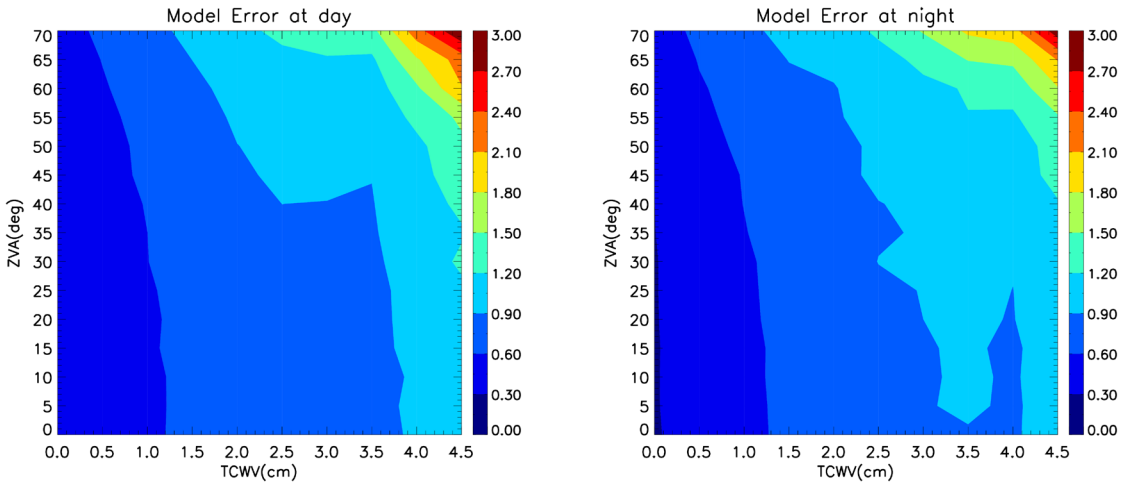

Figure 22 Enterprise LST model error distribution within class of TPW and ZVA for daytime (left) and nighttime (right), respectively

2.5.3.5 Overall LST uncertainty estimation

The overall LST uncertainty is calculated using equation 3.4. Figure 2-21 shows the histogram of overall global LST error and its components for the case scenario on Oct. 1st, 2019 for daytime (left) and nighttime (right). Note that the result is affected by the atmospheric conditions in the global distribution on the specific day. S_{lst} is found generally less than 2 K for daytime and 1.5 K for nighttime.

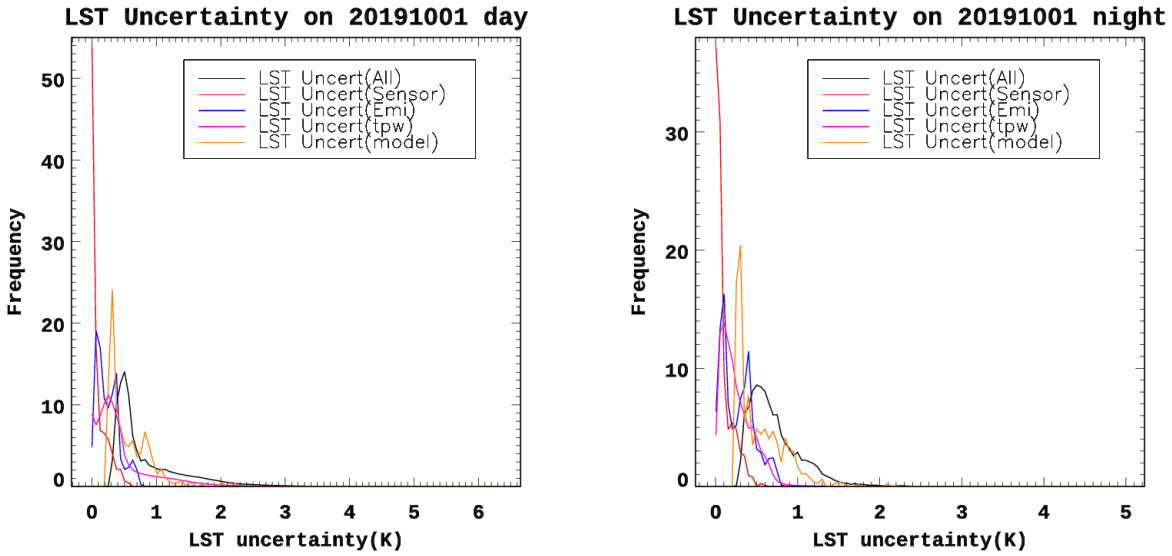

Figure 22 Histogram of global LST error and its components for the case scenario on Oct. 1st, 2019 for daytime (left) and nighttime (right)

According to Figure 2-21, the sensor noise generally has the smallest contribution, mostly less than 0.3 K, to the overall LST error. The largest errors are expected under the moist condition with high satellite viewing angles. Emissivity sensitivity is still an issue because the emissivity effect is coupled with the atmospheric absorption effect in the radiative transfer process; while the atmospheric absorption effect is linearized in the SW technique, the emissivity effect cannot be similarly linearized.
In the LST error propagation, we opted to ignore the error from SZA considering that the probability of having the wrong class of SZA is very low. However, the sensor view geometry may have significant impact on the variation of atmospheric absorption due to the radiative transfer path length increase from nadir to the edge of the scan. VIIRS has a wide swath of ~3060 km and the sensor zenith angle can reach 72 degree. For cases where very moist atmospheres are observed with high zenith angles, the linear combination of the split-window channels cannot reproduce the nonlinear path length effects (Freitas et al., 2010), which leads to the significant model error about 3 K as shown in Figure 2-20.

Finally, we emphasize that all the results discussed to this point assume perfect cloud detection. That is, all these results are for truly cloud clear pixels. Residual cloud effects in pixels detected as clear will introduce significant uncertainty to the LST retrievals.

2.6 Practical Considerations

2.6.1 Numerical Computation Considerations

The LST algorithm selected is mathematically simple and requires no complicated mathematical routines. In operations it will be robust and fast enough in terms of the algorithm latency requirement (< 15 minutes, goal) using current computer power. For storage consideration, LST values should be scaled in two-byte integers, with scale factors and offset defined in the attributes. Quality flags for each pixel value should be bit-flag definitions, to minimize data storage.

2.6.2 Programming and Procedural Considerations

Because of the algorithm simplicity, the LST algorithm requires small amount of code, with basic mathematical routines. However, since the LST algorithm requires ancillary datasets such as emissivity data and the total column water data, mapping of the ancillary datasets to the satellite pixel geolocation is necessary.

Because the retrieval is stratified by different atmospheric conditions (day/night, dry/moist) and viewing geometry, spatial discontinuity of the derived LST field is a concern. Although such discontinuity is not observed obviously in the proxy data tests, further verification should be performed to ensure it is not a real problem.

The primary adjustable parameters for the LST retrieval are the algorithm coefficients that are stratified for four atmospheric conditions. Threshold values for the dry, moist and very moist atmospheric conditions are adjustable in order to optimize the algorithm if needed. Source of ancillary datasets should be configurable for the best dataset. And finally, it should be kept in mind that metadata used for the product may be modified, reduced and added in late phase of the product generation.

The LST retrieval will be assessed and monitored. First, a set of quality control flags will be generated with the LST product for retrieval diagnostics, as is presented in Section 3.4. The quality control flags will indicate the retrieval conditions, including the land/non-land surfaces (i.e., land, snow, ice, inland water etc.), atmospheric water vapor status (i.e., dry, moist and very moist conditions), day and night, large view angle etc. LST maps and statistical information will be generated and reviewed for quality assessment.

2.6.3 Exception Handling

When LST cannot be retrieved due to conditions such as missing or bad SDR data, cloud-contaminated pixel, or sea-water pixel as indicated from the land sea mask, LST pixel values are set to fill. Availability of other ancillary datasets such as emissivity and water vapor will also be checked and the retrieval will be skipped if either is not available. In addition to this,

code is added to check the valid ranges of the input e.g. brightness temperature of band 15 and 16, emissivity etc. into the LST EDR. The valid ranges of these inputs are included into a separate file which is configurable and can be changed without having to recompile.

2.7 Validation

The selected algorithm (7) is verified through validation with in-situ observations and cross satellite comparisons using satellite data from multiple sensors with TIR split window channels, including VIIRS, the Spinning Enhanced Visible and Infra-red Imager (SEVIRI) onboard the European Meteosat Second Generation (MSG) satellite, the Moderate Resolution Imaging Spectroradiometer (MODIS) on Aqua satellite, and Advanced Himawari Imager (AHI) onboard Himawari 8 satellite. Algorithm coefficients for different sensor inputs are different due to their different central wavelengths and spectral response functions. The same simulation dataset and regression procedure are used, as described in Section 2.3.2, to generate the algorithm coefficients for each sensor, with its corresponding spectral characteristics. Algorithm 7, in this section, will be referred to as “the algorithm”.

2.7.1 Evaluation using ground observations

Considering the global representativeness and satellite spatial coverage, we collected the ground observations from SURFRAD, BSRN, and GMD for evaluations of the enterprise VIIRS LST; the data from Karlsruhe Institute of Technology (KIT) in Africa for evaluations of the SEVIRI LST generated using the enterprise LST algorithm, which will be referred to as “the enterprise SEVIRI LST”; the data from Australian and New Zealand Flux Research and Monitoring (OZFLux) for evaluations of the AHI LST generated using the enterprise algorithm, which will be referred to as “the enterprise AHI LST” in later chapters.

2.7.1.1 Ground data measurements

2.7.1.1.1 SURFRAD Data

The SURFRAD network has been operational in the United States since 1995. It provides high quality in situ measurements of upwelling and downwelling radiation, along with other meteorological parameters such as the atmospheric water vapor. A detailed description of the SURFRAD network and associated instrumentation can be found in Augustine *et al*. (2000; 2005). Three years (08/2012 to 07/2015) of data from seven SURFRAD stations (Table 2-10) are used.

Table 2-10 A brief introduction of the six SURFRAD stations whose data are used for the algorithm evaluation.

Site No.	Site Location	Lat(N)/Lon(W)	Surface Type (IGBP)
1	Pennsylvania State University, PA	40.72/77.93	Crop Land
2	Bondville, IL	40.05/88.37	Crop Land

3	Goodwin Creek, MS	34.25/89.87	Grass Land
4	Fort Peck, MT	48.31/105.10	Grass Land
5	Boulder, CO	40.13/105.24	Crop Land
6	Desert Rock, NV	36.63/116.02	Open Shrub Land
7	Sioux Falls, SD	43.73/96.62	Crop Land

The SURFRAD ground LST values were calculated from upwelling and downwelling radiation measurements, in the spectral range from 3 μm to 50 μm, obtained by a precise infrared radiometer (PIR). The SURFRAD PIR is calibrated annually using a laboratory blackbody so that its measurement estimates the total energy emitted from a blackbody rather than the instrument limited spectrum (Augustine *et al*., 2000; 2005).

2.7.1.1.2 BSRN data

The radiometric network BSRN was launched in 1992 by World Climate Research Programme (WCRP) to support the research projects of the WCRP and other scientific programs. BSRN provides typically 1-minute averaged short- and long-wave surface radiation fluxes. As of mid-2013, the data import is organized in so-called station-to-archive files, which contain all the data from one station collected during one month. Currently a total of over 7000 station-month datasets from 58 stations (Figure 2-22) are available in the World Radiation Monitoring Center (WRMC). Two sites, CAB site located in Cabauw, the Netherlands, and GOB site located in Gobabeb, Namibia, are selected based on the following criteria: availability of both upwelling and downwelling long wave radiation observations, temporal overlap with VIIRS measurements, and site thermal homogeneity (especially if a site is close to water body).

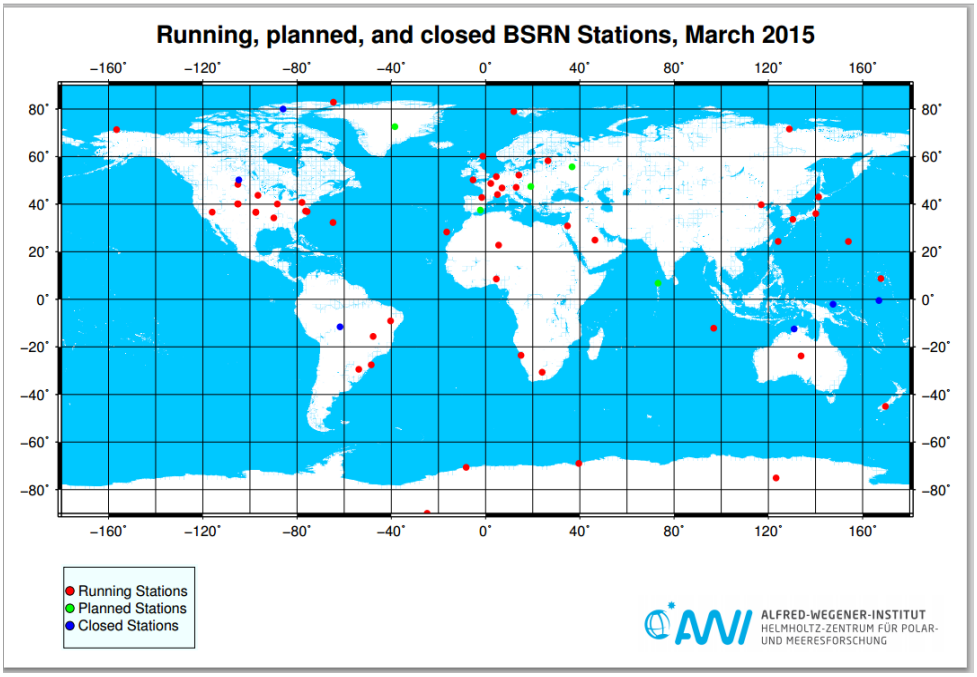

Source: http://bsrn.awi.de/fileadmin/user_upload/redakteur/Maps/BSRN-Station-Global.pdf

Figure 23 BSRN site maps

2.7.1.1.3 GMD data

GMD baseline observatories include 6 sites (Figure 2-23). Due to similar reasons explained in section for BSRN, only one site, Summit site in Greenland, is selected for LST validation. GMD also provides typically 1-minute averaged short- and long-wave surface radiation fluxes, in which the long wave radiation is used for ground LST calculation.

Figure 2-24 GMD site maps (http://www.esrl.noaa.gov/gmd/)

2.7.1.1.4 KIT data

Supported by the Land Surface Analysis - Satellite Applications Facility (LSA-SAF), KIT of Germany operates four permanent validation stations for evaluation of LST retrieved from TIR satellite measurements (Göttsche and Olesen, 2009; Olesen and Göttsche, 2009). In this study we used one month data in March 2012 over two sites: one is in Gobabeb, and the other one is in Heimat, Namibia (Figure 2-24a). Two down-looking Heitronics KT-15.85 IIP radiometers measure the surface-leaving radiance (9.6-11.5μm) from the gravel plain with the fields of view (FOV) about 13 m^2 each. A third radiometer (Kipp & Zonen CNR1) at the 2 m level measures sky radiance, in terms of broad-band shortwave (SW) and longwave (LW) radiative fluxes (Figure 2-24b). Brightness temperatures from the surface pointing radiometers are converted to radiances, which are then corrected for reflected downwelling radiance using the monthly mean surface emissivity extracted from the CIMSS baseline fit emissivity database for 11 μm and measured downwelling radiance. LST is then obtained from the corrected surface leaving radiances.

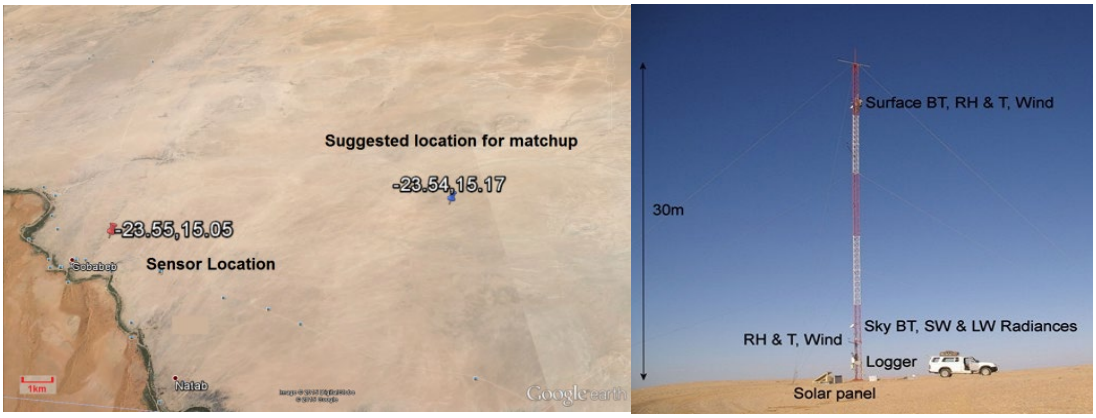

Figure 2-25 (a) is Geographic landscape in Gobabeb station in Namibia and (b) is the instrumentation for LST measurement: two radiometers measure the surface-leaving radiance (9.6–11.5 μm) from the gravel plain, which is highly homogenous over at least 2500 km^2.

2.7.1.1.5 OzFlux data

OzFlux is a network of micrometeorological flux stations located at various sites within Australia and New Zealand (Figure 2-25). OzFlux is part of an international network (FluxNet) of over 500 flux stations that is designed to provide continuous, long-term micrometeorological measurements to monitor the state of ecosystems globally.

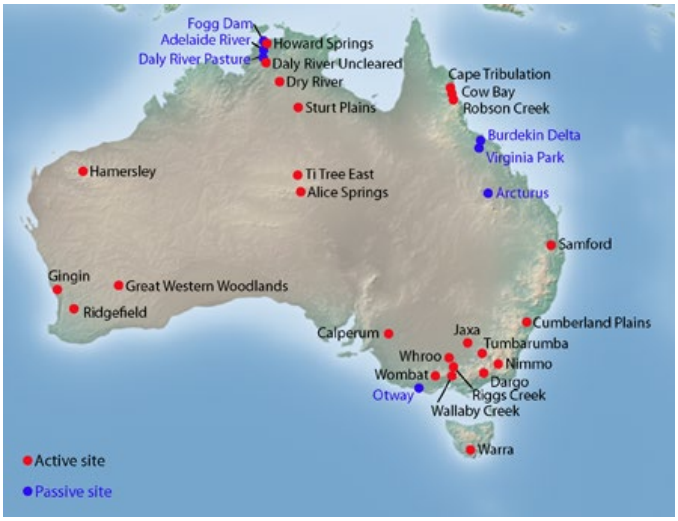

Name	Latitude	Longitude	Vegetation	Time zone
Alice Springs Mulga	-22.283	133.249	Woodland	Australia/Darwin
Cape Tribulation	-16.103	145.447	Forest	Australia/Brisbane
Dain tree	-16.238	145.427	Forest	Australia/Brisbane
Daly	-14.159	131.388	Woody Savanna	Australia/Darwin
Dry River	-15.259	132.371	Woody Savanna	Australia/Darwin
Great Western Woodlands	-30.191	120.654	Woodland	Australia/Perth
Howard Springs	-12.495	131.15	Woody savanna	Australia/Darwin
Riggs	-36.656	145.576	Pasture	Australia/Melbourne
Robson	-17.117	145.63	Forest	Australia/Brisbane
Sturt Plains	-17.151	133.35	Grasslands	Australia/Darwin
Ti Tree East	-22.287	133.64	Savanna	Australia/Darwin
Whroo	-36.673	145.029	Woodland	Australia/Melbourne
Yanco	-34.988	146.291	NA	Australia/Sydney

Figure 2-26 OzFlux monitoring site map and table (http://www.ozflux.org.au/monitoringsites/index.html)

OzFlux provides Meteorological data such as air temperature, humidity, wind speed and direction, and precipitation; radiation data such as incoming and outgoing shortwave and longwave, net radiation, and direct and diffuse shortwave; soil data such as soil heat flux, soil temperature and soil moisture etc. Same as SURFRAD, the long wave upwelling and downwelling measurements are used for ground LST calculation. In this study, two sites in Alice Springs Mulga (ASM) and in Ti Tree East (TTE) are selected for LST validation given that these two sites are relatively homogeneous in thermal flux.

2.7.1.2 Ground LST data calculation and matchup procedure

The data from SURFRAD, BSRN, GMD as well as OzFlux provides the long-wave downwelling and upwelling radiative fluxes. The in-situ surface skin temperature, Ts, can be estimated using the following equation

$$T_s = ((R^{\uparrow} - (1-\varepsilon)R^{\downarrow})/\sigma\varepsilon)^{1/4} \qquad (4.1)$$

Where $R^{\uparrow}$ and $R^{\downarrow}$ are upwelling and downwelling long wave fluxes respectively, ε is the surface broadband emissivity, and σ is Stefan-Boltzmann constant, i.e., 5.67051×10^{-8} $W \cdot m^{-2} \cdot K^{-4}$. Instead of using the fixed emissivity value for each site, the monthly emissivity is used to better characterize the emissivity change over sites. Both ground data and satellite data are quality controlled using the procedure described in Liu et al. (2015).

Two procedures are used for ground data quality control: the first applies the quality flag (QF) included in the original data, e.g., a QF of zero indicates that the corresponding data point is

good, having passed all QC checks; the other is the temporal variation test by checking the Standard Deviation (STD) of downwelling sky irradiance in the 30 minutes temporal interval centered at the observation time. A STD threshold value of 1.5 is used to remove the potential cloud contamination and signal noise and allow reasonable temporal variability.

To reduce cloud contamination and suboptimal atmospheric conditions, only the satellite data with confidently clear QF for cloud condition is used. In addition, the spatial variation test, *i.e.*, the STD of the neighboring 3 by 3 pixel brightness temperature of the channel at 11 μm centered at the matchup pixel, is applied as an additional cloud filter. The STD should be small over thermal homogeneous surfaces unless there is cirrus or cloud cover. The spatial variation test is widely used in LST validation studies. For example, Li *et al.* [2014] used the neighboring 5 × 5 box for MODIS LST validation. In this study, the threshold is set as 1.5 K, although it may be slightly higher (e.g., 1.75 K) for sites like Boulder [Yu et al., 2009b]. We intend to include all angle measurements in the validation and therefore the LST data quality flag is not applied as it includes the viewing zenith angle restriction.

For temperature-based (T-based) validation, the satellite LST and its in-situ counterpart data pair with smallest distance in both time and space is selected. For cross-sensor comparison, the temporal difference is controlled within 10 minutes.

2.7.1.3 Ground validation results

2.7.1.3.1 Match-up VIIRS LST and Station Observation Data

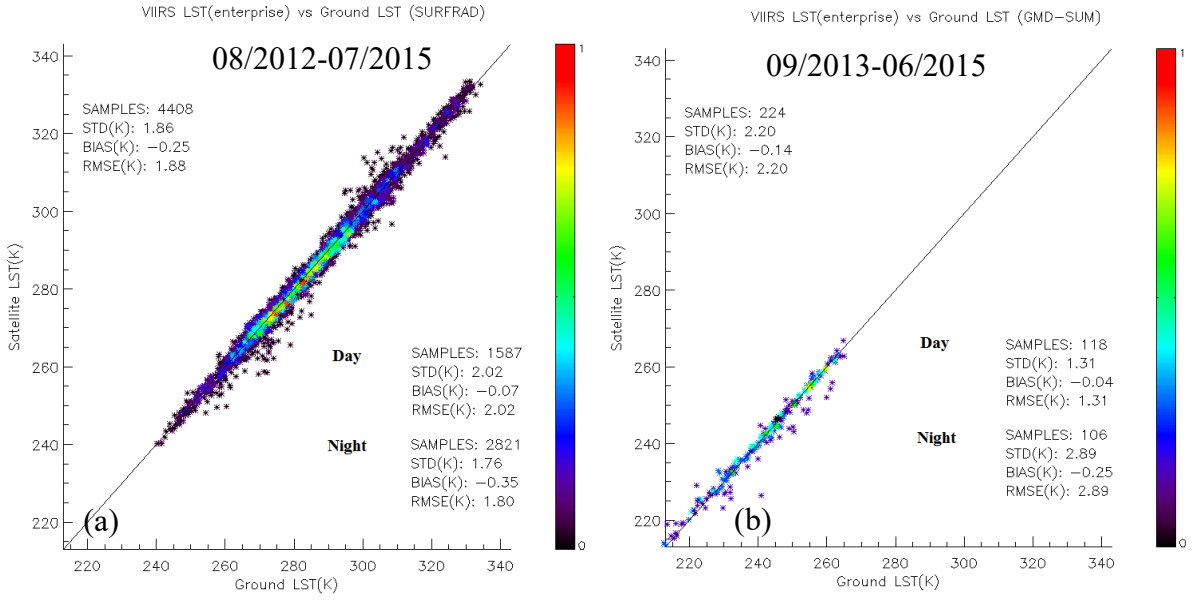

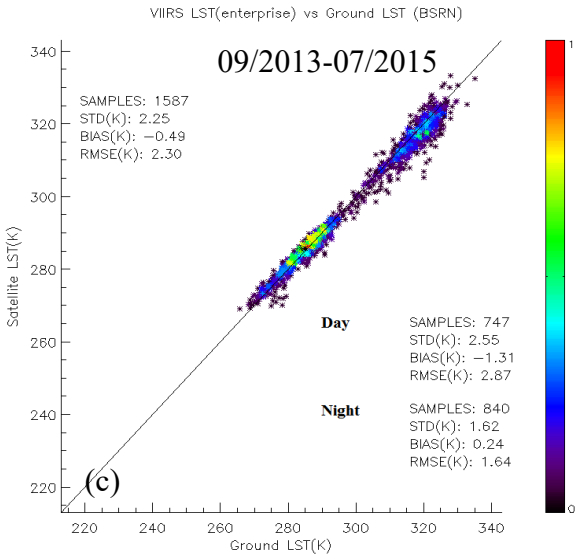

Figure 2-27 Enterprise VIIRS LST against ground data from (a) SURFRAD, (b) GMD, and (c) BSRN.

The match-up of the enterprise VIIRS LST and ground observations was carried out on all cloud free pixels. The result for SURFRAD includes 7 sites with the biggest sample size (Figure 2-26a), followed by that for BRSN (Figure 2-26b) with two sites, and GMD (Figure 2-26c) with only one site. A better agreement is found at nighttime than at daytime, with the exception of the GMD result, due to a higher possibility of cloud contamination over snow/ice surface at nighttime even with the comprehensive cloud screening procedure.

2.7.1.3.2 Match-up SEVIRI LST and ground measurements from KIT

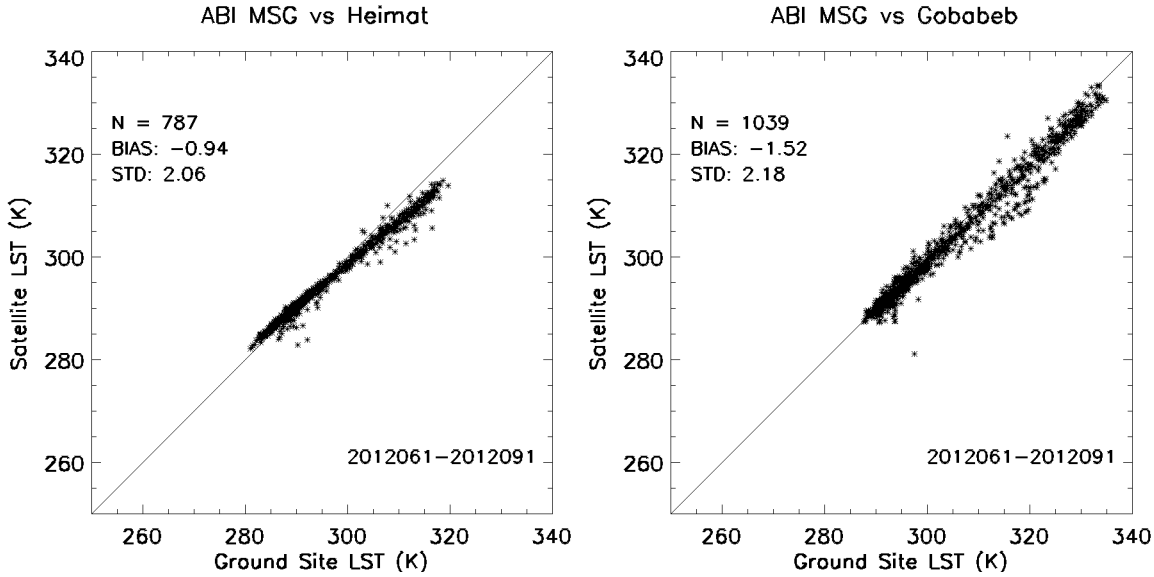

Figure 2-28 SEVIRI LST against ground data from KIT over Gobabeb site (right) and Heimat site (left) for March, 2012.

The relatively large cold bias between the ground and the satellite data has been noted as shown in Figure 2-27. The cause of the bias is unknown yet. Further investigations will be conducted during the period of intensive algorithm evaluations.

2.7.1.3.3 Match-up AHI LST and ground measurements from OzFlux

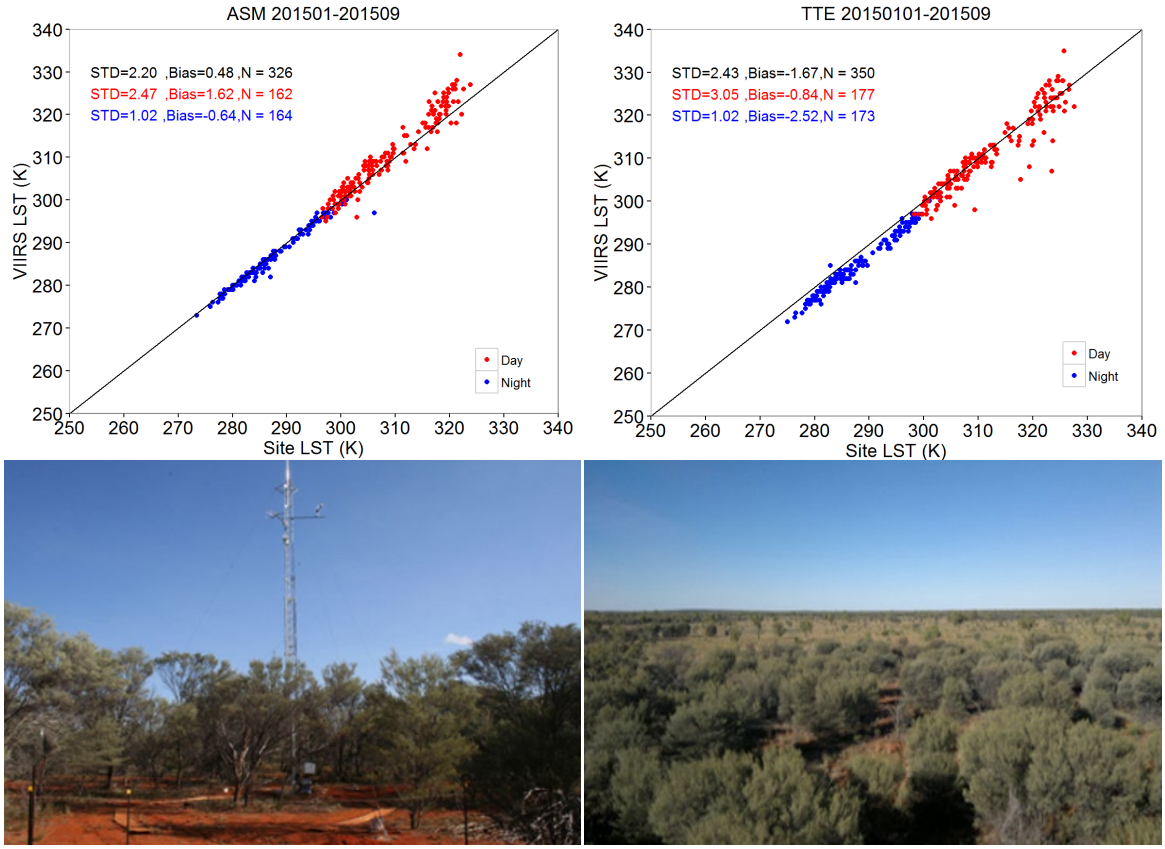

Figure 2-29 AHI LST against ground data from OzFlux over TTE ASM site (left) and site (right) from January to September, 2015

The much better agreement between the ground and the satellite data at nighttime compared to that at daytime has been found though the LST underestimation is observed at TTE site (Figure 2-28).

2.7.2 Cross satellite evaluations

2.7.2.1 Enterprise VIIRS LST and SEVIRI LST

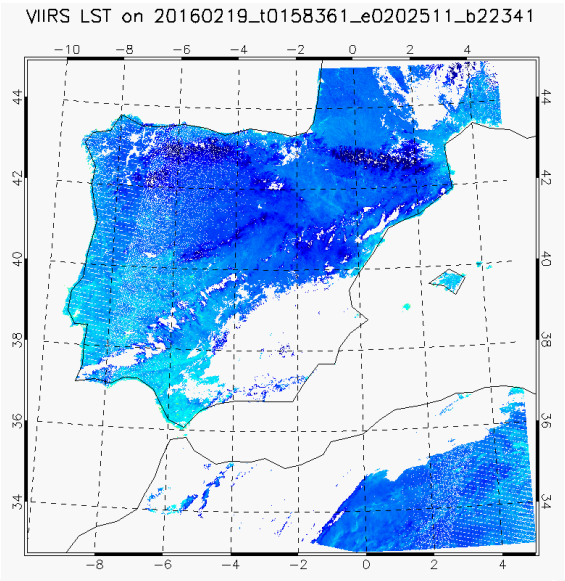
VIIRS LST on 20160219_t0158361_e0202511_b22341

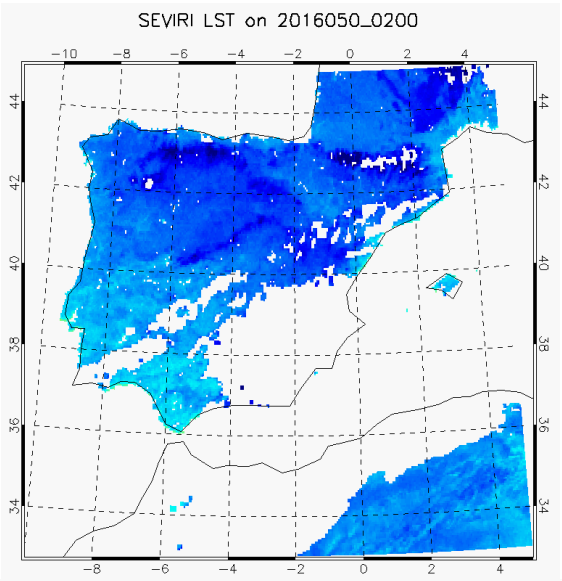
SEVIRI LST on 2016050_0200

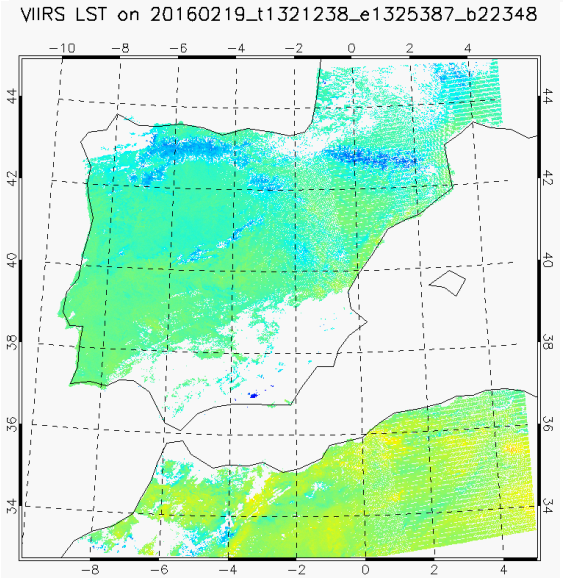
VIIRS LST on 20160219_t1321238_e1325387_b22348

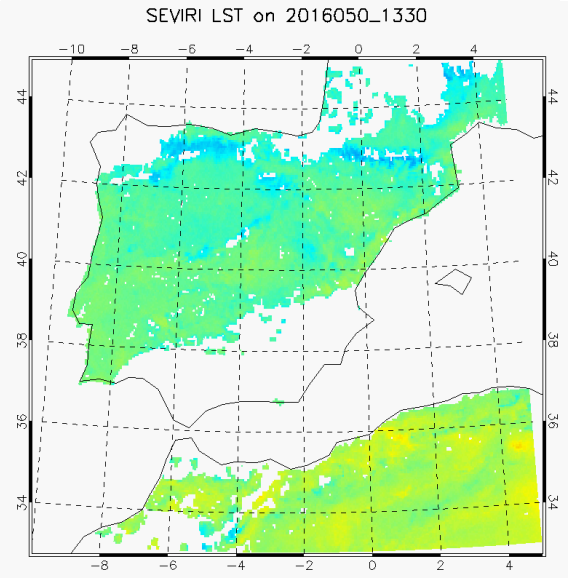
SEVIRI LST on 2016050_1330

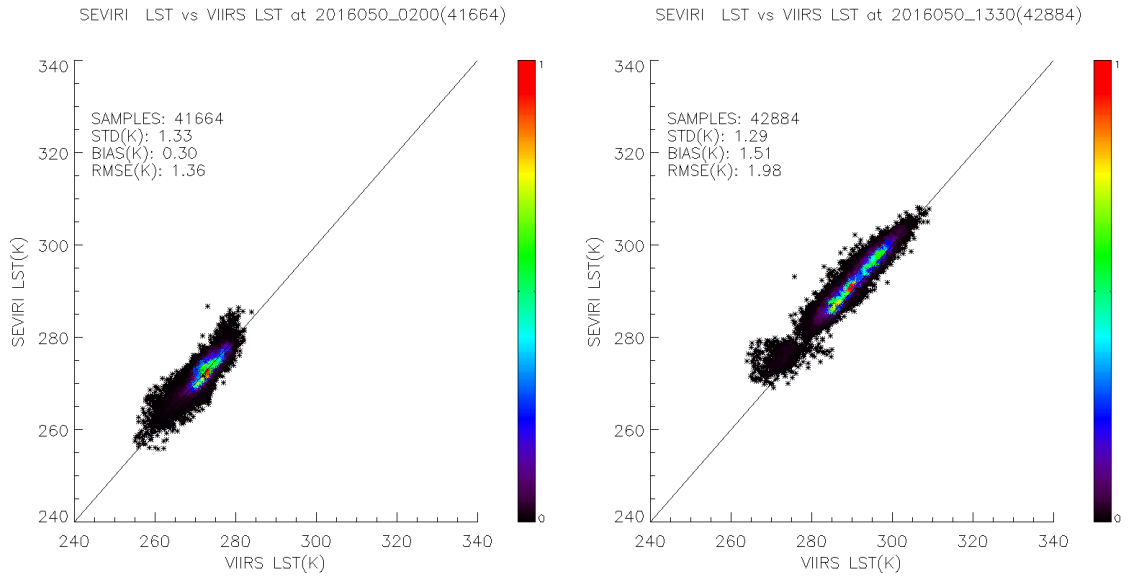

Figure 30 Enterprise VIIRS LST versus enterprise SEVIRI LST over two scenes on Feb. 19 UTC 02:00 (nighttime) and UTC 13:25 (daytime) over Iberian Peninsula area. The cross-comparison results are shown in the scatter plot

A slightly better agreement is found at nighttime compared to that at daytime (Figure 2-29). The enterprise SEVIRI LST is found on average 1.5 K warmer than the enterprise VIIRS LST, similar to their brightness temperature difference at around 11μm. It is worth mentioning that all finer resolution VIIRS LSTs falling in the same coarser resolution SEVIRI pixel are averaged to match the LST from the latter. Therefore, the mapping uncertainty as well as the sub pixel cloud will potentially affect the comparison results.

2.7.2.2 Enterprise VIIRS LST and AQUA LST

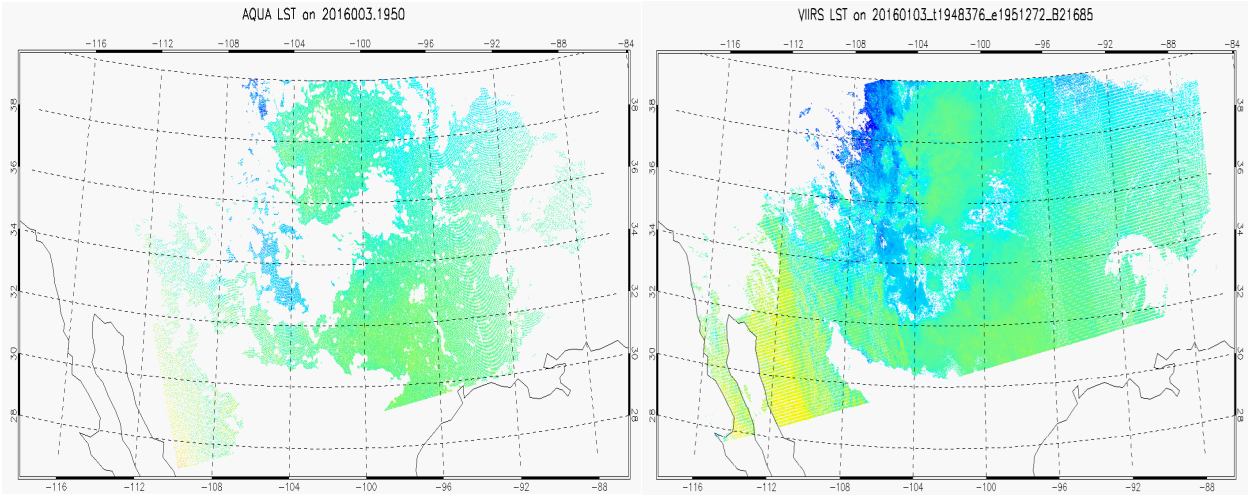

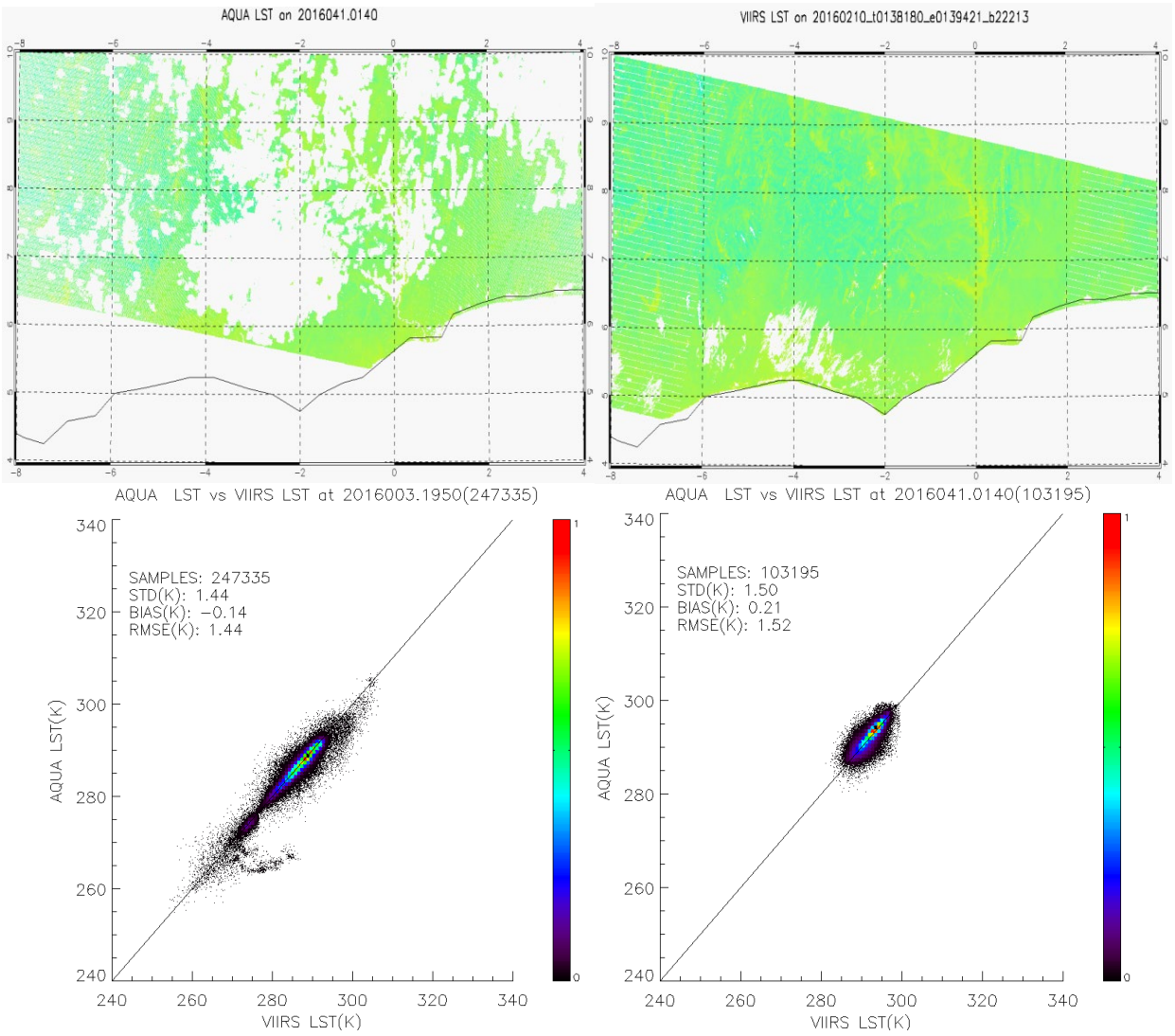

Figure 31 Enterprise VIIRS LST versus enterprise MODIS AQUA LST over two scenes on Jan. 3 2016 at UTC 19:50(daytime) over US and Feb. 10, 2016 at UTC 01:40 (nighttime) over. The cross-comparison results are shown in the scatter plot.

For the cross comparison between two sensors with similar footprints, the closest neighbor is used to select the comparable pixel. Besides the difference in the sensor data, the viewing geometry as well as the cloud mask accuracy will affect the comparison results. The result in Figure 2-30 indicates an overall close agreement between the enterprise VIIRS LST and MODIS LST estimation. But some noises are observed for the daytime case, which might be due to the cloud contamination.

2.7.2.3 Enterprise VIIRS LST and AHI LST

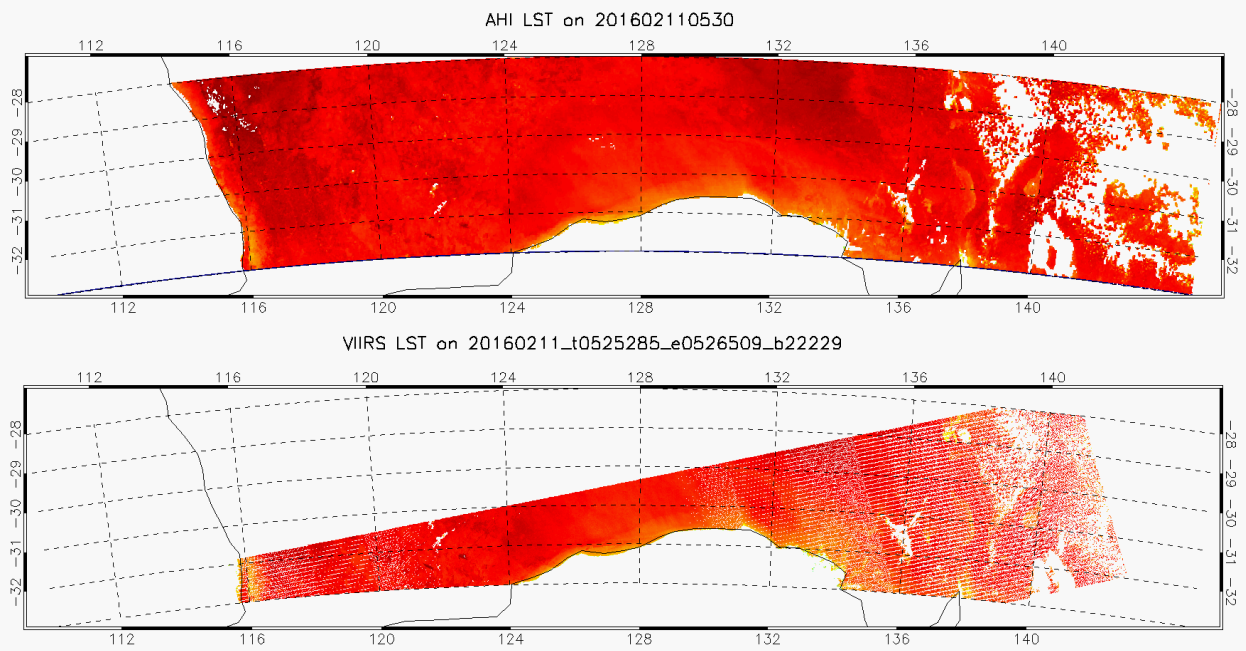
AHI LST on 201602110530
VIIRS LST on 20160211_t0525285_e0526509_b22229

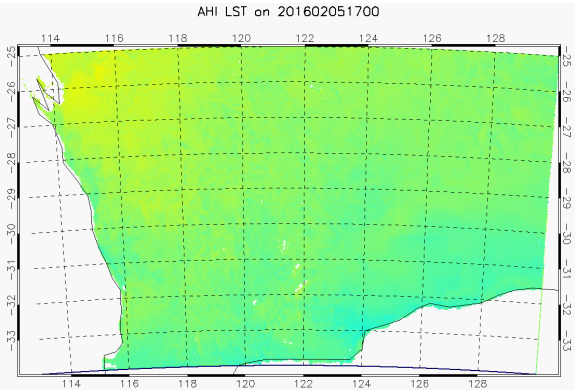
AHI LST on 201602051700

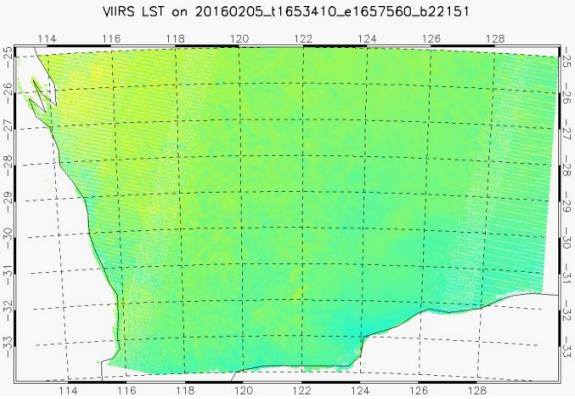
VIIRS LST on 20160205_t1653410_e1657560_b22151

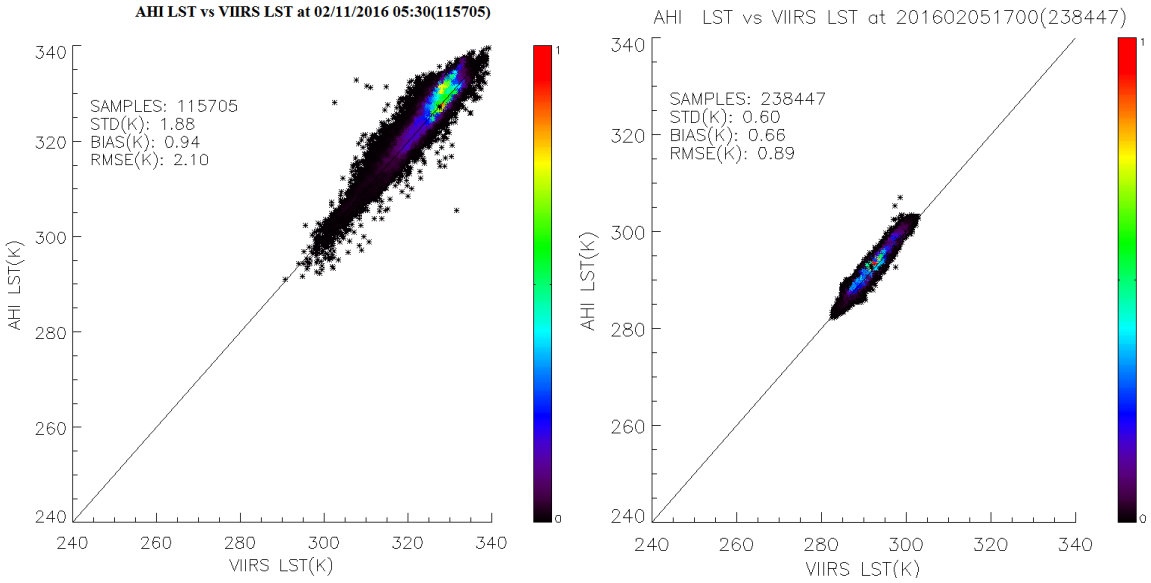

Figure 32 Enterprise VIIRS LST versus enterprise AHI LST over two scenes on Feb. 11, 2016 at UTC 05:30(daytime) and Feb. 5, 2016 at UTC 17:00 (nighttime). The cross-comparison results are shown in the scatter plot.

The same matchup method used in the cross comparison between VIIRS and SEVIRI LSTs is applied. For the two scenes cases, the nighttime comparison shows a much better agreement compared to the daytime case (Figure 2-31). The bias is found consistent with the sensor data difference between VIIRS and AHI. The noisy matchups particularly those with over 10 K difference is likely caused by the cloud contamination effect.

2.7.3 Error Budget Summary

In summary, we provided a quantitative assessment of the enterprise algorithm with a variety of test datasets, including the enterprise VIIRS LST, SEVIRI LST, AQUA MODIS LST as well as AHI LST. The assessment results indicate that the selected enterprise LST algorithm can be used for multiple sensors. And the evaluation results demonstrate it can meet both the accuracy (1.4 K) and precision (2.5 K) requirements.

A variety of sources may introduce errors in the satellite LST retrieval, yet it is very hard to quantitatively identify each one, as most of the error sources are coupled to each other. In our algorithm development, we tried to reduce the LST retrieval error by stratifying the algorithm coefficients with different atmospheric moisture conditions, and with different view zenith angle ranges and applying emissivity explicitly in the retrieval formula. The test and evaluation results indicate that the algorithm can meet the accuracy and precision requirements.

However, it must be pointed out that several issues remain unsolved in the algorithm and in the test and evaluation process. First, the algorithm is still sensitive to the surface emissivity uncertainty. A 0.015 emissivity uncertainty may introduce about 1 K (Figure 2-17) LST retrieval error when the atmosphere is relatively moist. Second, the residual of the atmospheric correction can be up to 0.9 K (Table 2-18), and additional errors may be introduced if the water vapor information is not right (Figures 2-18). Errors will also be introduced in the algorithm coefficient generation due to uncertainties from the MODTRAN radiative transfer model.

In the algorithm evaluation process, as mentioned earlier, there are several issues that should be further studied in the match-up dataset comparisons. Difference between the satellite pixel-size measurement and the ground spot-size measurement must be characterized for a high quality validation procedure.

Cloud contamination remains a problem even with stringent cloud filtering procedures. The problem is particularly significant over nighttime snow surface according to the validation practices conducted over Summit site in Greenland. Note that due to the unavailability of the ECM, above ground validation and cross satellite comparison are based on the IDPS VIIRS cloud mask. It has been observed that the enterprise cloud mask and IDPS cloud mask are quite different, which may affect the validation results.

3 ASSUMPTIONS AND LIMITATIONS

3.1 Performance Assumptions

The following assumptions have been made in developing and estimating the performance of the LST retrieval algorithm and products, including proposed mitigation strategies in parentheses.

- The ECM is available at the time of LST retrieval (Use alternative built-in algorithm to identify cloudy pixels)
- High quality dynamic land surface emissivity dataset is available
- The NCEP analysis and forecast water vapor are available
- SDR data is calibrated and navigated, and are not distorted (set quality flag to bad pixels and no LST retrieval is performed).

The LST retrieval algorithm is applicable only on cloudless pixels. The impact on LST due to roughness and/or structure of land surface, the emissivity directional feature and its variation in a pixel are not handled in the algorithm. The retrieved LST value is an effective land surface skin temperature over isothermal mixed pixel. The retrieval accuracy may be degraded significantly in regions with heavy atmospheric water vapor loading (e.g. > 5.0 g/cm^2) and

large viewing angles. Also, the retrieval may be questionable in regions with very low LST and where the surface air temperature is 15 K higher or lower than LST.

From VIIRS SDR long term monitoring and validation results, VIIRS on orbit performance is well characterized and meets specifications; noise is small and stable; accuracy is well characterized for thermal emissive bands; geolocation uncertainties for M-bands are ~70m at nadir meeting specifications are nadir and edge of scan[Cao et al., 2013]. The performance of JPSS 1 is expected to be as good as SNPP. The algorithm coefficient might be calibrated or tuned using the real spectral response function.

3.2 Potential Improvements

We recently included the SEEBOR profiles into our simulation database. The Seebor V5.0 consists of 15704 global profiles of temperature, moisture, and ozone at 101 pressure levels for clear sky conditions in which there are 9136 profiles over land. The profiles are taken from NOAA-88, an ECMWF 60L training set, TIGR-3, ozonesondes from 8 NOAA Climate Monitoring and Diagnostics Laboratory (CMDL) sites and radiosondes from 2004 in the Sahara desert. (Borbas et al., 2005). The Seebor profiles over land represents a variety of atmospheric conditions, spanning a column water vapor range from 0.2 to 7.5 g/cm2 , a surface air temperature range from 200 K to 319 K and the LST range from 204 K to 337 K. It provides an opportunity for very low and very high temperature derivation. The improvement will involve the refinement of the enterprise LST LUT based on the SEEBOR simulation database. The LST performance enhancements over very low and very high temperature is expected. In addition, the advances in emissivity estimation will further improve the LST accuracy.

4 REFERENCES

Anderson, M.C.; Kustas,W.P.; Norman, J.M.; Hain, C.R.; Mecikalski, J.R.; Schultz, L.; Gonzalez-Dugo, M.P.; Cammalleri, C.; d'Urso, G.; Pimstein, A.; Gao, F. Mapping daily evapotranspiration at field to continental scales using geostationary and polar orbiting satellite imagery. Hydro. Earth Sys. Sci. 2011, 15, 223–239.

Anderson, M.C.; Allen, R.G.; Morse, A.; Kustas, W.P. Use of Landsat thermal imagery in monitoring evapotranspiration and managing water resources. Remote Sens. Environ. 2012, 122, 50–65.

Augustine, J. A., DeLuisi, J. J., Long, C. N., SURFRAD- A National Surface Radiation Budget Network for Atmospheric Research, Bull. Amer. Meteor. Soc., 81, 2341-2357, 2000.

Augustine, J. A., Hodges, G. B., Cornwall, C. R., Michalsky J. J. and Medina, C. I., An Update on SURFRAD- The GCOS Surface Radiation Budget Network for the Continental United States, J. Atmos. Oceanic Technol., 22, 1460-1472, 2005.

Baker N., Land Surface Temperature Visible/Infrared Image radiometer Suite Algorithm Theoretical Basis Document, http://www.star.nesdis.noaa.gov/jpss/documents/ATBD/D0001-M01-S01-022_JPSS_ATBD_VIIRS-LST_A.pdf

Becker, F., and Li, Z. L., Towards a local split window method over land surfaces, Int. J. Remote Sensing, vol. 11, pp. 369-393, 1990.

Berk, A., Anderson, G.P., Acharya, P.K., Bernstein, L.S., Muratov, L., Lee, J., Fox, M.J., Adler-Golden, S.M., Chetwynd, J.H., Hoke, M.L., Lockwood, R.B., Cooley, T.W. and Gardner, J.A., MODTRAN5: a Reformulated Atmospheric Band Model with Auxiliary Species and Practical Multiple Scattering Options, Proc. SPIE Int. Soc. Opt. Eng. 5655, 88 (2005).

Borbas, E. E., Moy, L., Seemann, S. W., Knuteson, R. O., Antonelli, P., Li, J., Huang, H-L, Trigo, I., Meteorologia, I. de, Zhou, L., A Global Infrared Land Surface Emissivity Database and Its Validation, P2.7, AMS Annual meeting, New Orleans, January, 2008.

Cadeddu, MP, Liljegren, JC, and Turner, DD., The Atmospheric Radiation Measurement (ARM) program network of microwave radiometers: Instrumentation, data, and retrievals, Atmospheric Measurement Techniques 6: 2359-2372, doi:10.5194/amt-6-2359-2013 (2013).

Cao, C.Y., Xiong, J., Slawomir, B., Liu, Q., Sirish, U., Shao, X., Bai, Y. and Weng, F., Suomi NPP VIIRS sensor data record verification, validation, and long-term performance monitoring, Journal of Geophysical Research: Aemosphere, Vol. 118, 11,664–11,678, doi: 10.1002/2013JD020418, 2013.

Caselles, V., Coll, C. and Valor, E., Land surface temperature determination in the whole Hapex Sahell area from AVHRR data, Int. J. Remote Sens., vol. 18, no. 5, pp. 1009–1027, 1997.

Chédin, A. and Scott N.A., The impact of spectroscopic parameters on the composition of the Jovian atmosphere discussed in connection with recent laboratory, earth and planetary observation programs. J. Quant. Spectrosc. Radiat. Transfer 32, pp. 453-461, doi: 10.1016/0022-4073(84)90040-2(1985)

Chevallier F., Chéruy F., Scott N.A. and Chédin A., A neural network approach for a fast and accurate computation of longwave radiative budget. J. of Applied Meteorology 37:11, 1385-1397. (1998)

Claud C., Scott N.A., Chédin A., Gascard J.C., Assessment of the accuracy of atmospheric temperature profiles retrieved from TOVS observations by the "3I" method in the European Arctic ; applications to mesoscale weather analysis, J. of Geophysical Research96, n° D2, pp. 2875-2887, doi:10.1029/90JD02413 (1991)

Coll, C., Valor, E., Schmugge, T. and Caselles, V., A procedure for estimating the land surface emissivity difference in the AVHRR channels 4 and 5, Remote Sensing Application to the Valencian Area, Spain, 1997.

Coll, C., SOBRINO, J. A., Valor, E., On the atmospheric dependence of the split-window equation for land surface temperature, International Journal of Remote Sensing, Volume 15, Issue 1, 105-122, 1994

Coll, C., Caselles, V., Galve, J. M., Valor, E., Niclòs, R., Sanchez, J. M., et al., Ground measurements for the validation of land surface temperatures derived from AATSRand MODIS data, Remote Sensing of Environment, 97, 288–300, 2005..

Coll, C., Galve, J. M., Sanchez, J. M., & Caselles, V., Validation of Landsat-7/ETM+ thermal-band calibration and atmospheric correction with ground-based measurements, IEEE Transactions on Geoscience and Remote Sensing, 48, 547–55, 2010.

Coll, C., Valor, E., Galve, J.M., Mira, M., Bisquert, M., García-Santos, V., et al., Long-termaccuracy assessment of land surface temperatures derived from the Advanced Along-Track Scanning Radiometer, Remote Sensing of Environment, 116, 211–225, 2012.

Dash, P., Gottsche, F. M., Olesen, F. S., & Fischer, H., Land surface temperature and emissivity estimation from passive sensor data: theory and practice-current trends, International Journal of Remote Sensing, 23, 2563–2594, 2002.EUMETSAT homepage, http://www.eumetsat.int/groups/ops/documents/document/pdf_ten_052562_msg1_spctrsp.pdf

Freitas, SC, Trigo, IF, Bioucas-Dias, JM and Gottsche, FM, Quantifying the uncertainty of land surface temperature retrievals from SEVIRI/Meteosat, IEEE Transactions on Geoscience and Remote Sensing 48 (1), 523-534 (2010)

Galleguillos M, Jacob F, Prévot L, Frenchc A, Lagacheriea P., Comparison of two temperature differencing methods to estimate daily evapotranspiration over a Mediterranean vineyard watershed from ASTER data, Remote Sensing of Environment. 115 1326, 2011.

Galve, J.M., Coll, C., Caselles, V. and Valor, E., An Atmospheric Radiosounding Database for Generating Land Surface Temperature Algorithms, IEEE Transactions on Geoscience and Remote Sensing, Vol. 46, No. 5, May 2008

Göttsche, F. and Olesen F., A SIMPLE PHYSICALLY BASED MODEL OF DIURNAL CYCLES OF LAND SURFACE TEMPERATURE, extended abstract submitted to EUMETSAT Meteorological Satellite Conference, held in Bath, U.K., 21-25 September 2009.

Göttsche F., Olesen F., Trigo I.F., Bork-Unkelbach A. and Martin M.A., Long Term Validation of Land Surface Temperature Retrieved from MSG/SEVIRI with Continuous in-Situ Measurements in Africa, Remote Sensing, doi:10.3390/rs8050410 May 2016.

Guillevic, P. C., Privette, J. L., Coudert, B., Palecki, M. A., Demarty, J., Ottlé, C., et al. (2012). Land Surface Temperature product validation using NOAA's surface climate observation networks-Scaling methodology for the Visible Infrared Imager Radiometer Suite (VIIRS). Remote Sensing of Environment, 124, 282–298.

Hook, S. J., Gabell, A. R., Green, A. A., & Kealy, P. S. (1992). A comparison of techniques for extracting emissivity information from thermal infrared data for geologic studies. Remote Sensing Environment, 42, 123–135.

Hook, S. J., Vaughan, R. G., Tonooka, H., & Schladow, S. G. (2007). Absolute radiometric in-flight validation of mid infrared and thermal infrared data from ASTER and MODIS on the Terra spacecraft using the lake Tahoe, CA/NV, USA, Automated Validation Site. IEEE Transactions Geoscience and Remote Sensing, 45, 1798–1807.

Hulley, G. C., Hook, S.J., E. Abbott, N. Malakar, T. Islam, M. Abrams, 2015, The ASTER Global Emissivity Dataset (ASTER GED): Mapping Earth's emissivity at 100 meter spatial scale, Geophysical Research Letters, 42(19), 7966-7976.

Hulley, G. C., & Hook, S. J. (2009a). Intercomparison of versions 4, 4.1 and 5 of the MODIS Land Surface Temperature and Emissivity products and validation with laboratory measurements of sand samples from the Namib desert, Namibia. Remote Sensing of Environment, 113, 1313–1318.

Hulley, G. C., & Hook, S. J. (2009b). The North American ASTER Land Surface Emissivity Database (NAALSED) Version 2.0. Remote Sensing of Environment, 113, 1967–1975.

Hulley, G. C., & Hook, S. J. (2011). Generating consistent land surface temperature and emissivity products between ASTER and MODIS data for Earth science research. IEEE Transactions on Geoscience and Remote Sensing, 49, 1304–1315.

Hulley, G. C., Hook, S. J., & Baldridge, A. M. (2009). Validation of the North American ASTER Land Surface Emissivity Database (NAALSED) version 2.0 using pseudo-invariant sand dune sites. Remote Sensing of Environment, 113, 2224–2233.

Hulley, G., Hook, S., Hughes, T., Moderate Resolution Imaging Spectroradiometer (MODIS) MOD21 Land Surface Temperature and Emissivity Algorithm Theoretical Basis Document, August, 2012.

Karnieli, A., Agam, N., Pinker, R.P., Anderson, M., Imhoff, M. L., Gutman, G.G., Panov, N. and Goldberg, A., Use of NDVI and Land Surface Temperature for Drought Assessment: Merits and Limitations, DOI: http://dx.doi.org/10.1175/2009JCLI2900.1, Journal of Applied Meteorology and Climatology, 2010.

Li, S.; Yu, Y.; Sun, D.; Tarpley, D.; Zhan, X.; Chiu, L. Evaluation of 10 year AQUA/MODIS land surface temperature with SURFRAD observations. Int. J. Remote Sens. 2014, 35, 830–856.

Laszlo, I. and Liu, H. (2016), EPS Aerosol Optical Depth (AOD) Algorithm Theoretical Basis Document, available at

https://www.star.nesdis.noaa.gov/jpss/documents/ATBD/ATBD_EPS_Aerosol_AOD_v3.0.1.pdf

Li, H.; Sun, D.; Yu, Y.; Wang, H.; Liu, Y.; Liu, Q.; Du, Y.; Wang, H.; Cao, B. Evaluation of the VIIRS and MODIS LST products in an arid area of Northwest China. Remote Sens. Environ. 2014, 142, 111–121.

Li, Z-L, and F. Becker, Feasibility of land surface temperature and emissivity determination from AVHRR data, Remote Sensing of Environment, vol. 43, pp. 67-85, 1993.

Li, Z.; Tang, B.; Wu, H.; Ren, H.; Yan, G.; Wan, Z.; Trigo, I.F.; Sobrino, J.A. Satellite-derived land surface temperature: current status and perspectives. Remote Sens. Environ. 2013, 131, 14–37.

Liu, Y., Yu, Y., Yu, P., Göttsche, F. M. & Trigo, I.F. Quality Assessment of S-NPP VIIRS Land Surface Temperature Product. Remote Sens. 2015, 7(9), pp12215-12241; doi: 10.3390/rs70912215

McMillin, L. M., Estimation of sea surface temperatures from two infrared window measurements with different absorption, Journal of Geophysical Research 80 (C36), pp. 5113–5117, 1975.

McMillin, L. M., and D. S. Crosby, Theory and validation of multiple window sea surface temperature technique, J. Geophys. Res., 89, 3655-3661, 1984.

Meng, C.L.; Li, Z.-L.; Zhan, X.; Shi, J.C.; Liu, C.Y., Land surface temperature data assimilation and its impact on evapotranspiration estimates from the common land model. Water Res. Res. 2009, 45, W02421.

Norman, J. M., and F. Becker, Terminology in thermal infrared remote sensing of natural surfaces, Remote Sensing Rev. 12:159-173, 1995.

Olesen, F.S. and Göttsche, F.M., Validation of Land Surface Temperature Obtained from Meteosat-MRITI and Seviri with In-situ Measurements, , extended abstract submitted to EUMETSAT Meteorological Satellite Conference, held in Bath, U.K., 21-25 September 2009.

Prata, A. J., and C. M. R. Platt, Land surface temperature measurements from the AVHRR, in Proc. 5th AVHRR Data Users Conf., Tromso, Norway, Jun. 25–28, pp. 438–443. EUM P09, 1991.

Prata, A. J., Land surface temperatures derived from the AVHRR and the ATSR, 1, Theory, J. Geophys. Res., 98(D9), 16,689–16,702. 1993.

Prata, A. J., Land surface temperatures derived from the AVHRR and the ATSR, 2, Experimental results and validation of AVHRR algorithms, J. Geophys. Res., 99(D6), 13,025–13,058. 1994.

Price, J. C., Land surface temperature measurements from the split window channels of the NOAA-7/AVHRR, J. Geophys. Res., vol. 89, pp. 7231–7237, 1984.

Rajasekar, U.; Weng, Q. Urban heat island monitoring and analysis by data mining of MODIS imageries. ISPRS J. Photogramm. Remote Sens. 2009, 64, 86–96.

Reale, T., B. Sun, F. H. Tilley, and M. Pettey, 2012: The NOAA Products Validation System (NPROVS). J. Atmos. Oceanic Technol., 29, 629–645.

Rhee, J., Im, J., & Carbone, G.J. (2010). Monitoring agricultural drought for arid and humid regions using multi-sensor remote sensing data. Remote Sensing of Environment, 114, 2875-2887

Seemann, S.W., E. E. Borbas, R. O. Knuteson, G. R. Stephenson, H.-L. Huang, Development of a Global Infrared Land Surface Emissivity Database for Application to Clear Sky Sounding Retrievals from Multi-spectral Satellite Radiance Measurements. J. Appl. Meteor. Climatol., Vol. 47, 108-123, 2008.

Sellers, P. J., F. G. Hall, G. Asrar, D.E Strebel, and R. E. Murphy, The first ISLSEP field experiment (FIFE), Bull. Amer. Meteorol. Soc., Vol. 69, no. 1, 22-27, 1998.

Snyder, W. C., Z. Wan, and Y. Z. Feng, Classification-based emissivity for land surface temperature measurement from space, Int. J. Remote Sensing, vol. 19, no. 14, pp. 2753-2774, 1998.

Sobrino, J. A., Z. L. Li, M. P. Stoll, and F. Becker, Improvements in the split-window technique for land surface temperature determination, IEEE Trans. Geosci. Remote Sens., vol. 32, no. 2, pp. 243–253, Mar. 1994.

Sobrino, J. A., Z. L. Li, M. P. Stoll, and F. Becker, Determination of the surface temperature from ATSR data, in Proc. 25th Int. Symp. Remote Sens. Environ., Graz, Austria, Apr. 4–8, pp. II-19–II-109, 1993.

Sun, D. and Pinker, R.T. Estimation of land surface temperature from a Geostationary Operational Environmental Satellite (GOES-8). Journal of Geophysical Research, D, Atmospheres v.108, no. D11, 3 June 2003.

Sun, D. L., R. T. Pinker, J. B. Basara, Land surface temperature estimation from the next generation of Geostationary Operational Environmental Satellites: GOES M-Q, J. Appl. Meteorol. 43, pp. 363-372, 2004.

Sun, D., and R. Pinker, Case study of soil moisture's effect on land surface temperature retrieval, IEEE Trans. Geos. Remote Sens. Lett., 1 (2), 127-130, 2004.

Sun, J., Salvucci, G.D., and Entekhabi D., Estimates of evapotranspiration from MODIS and AMSR-E land surface temperature and moisture over the Southern Great Plains, Remote Sensing of Environment, vol. 127,pp. 44-59, Dec. 2012.

Trigo, I., Freitas, S., Bioucas-Dias, J., Barroso, C., Monteiro, I., Viterbo, P., Algorithm Theoretical Basis Document for Land Surface Temperature (LST) Products: LSA-4(MLST), June 2009.

Trigo I.F., Boussetta S., Viterbo P. , Balsamo3 G., Beljaars A., Sandu I., Comparison of model land skin temperature with remotely sensed estimates and assessment of surface-atmosphere coupling ,Journal of Geophysical Research Atmospheres, 120(23), DOI: 10.1002/2015JD023812, 2015.

Ulivieri, C., and G. Cannizzaro, Land surface temperature retrievals from satellite measurements, Acta Astronaut., vol. 12, no. 12, pp. 985–997, 1985.

Ulivieri, C., M. M. Castronouvo, R. Francioni, and A. Cardillo, A SW algorithm for estimating land surface temperature from satellites, Adv. Space Res., vol. 14, no. 3, pp. 59–65, 1992.

Voogt, J. A., & Oke, T. R. (2003). Thermal remote sensing of urban climates. Remote Sensing of Environment, 86, 370–384.

Walton, C. C., Pichel, W. G., Sapper, J. F., and May, D. A.,"The development and operational application of non-linear algorithms for the measurement of sea surface temperatures with the NOAA polar-orbiting environmental satellites, Journal of Geophysical Research, 103, 27 999–28 012, 1998.

Wan, Z., and J. Dozier, A generalized split-window algorithm for retrieving land-surface temperature measurement from space, IEEE Trans. Geosci. Remote Sensing, vol. 34, pp. 892–905, 1996.

Wan, Z., MODIS Land-Surface Temperature Algorithm Basis Document (LST ATBD): version 3.3, (April 1999).

Wan, Z., Wang, P., and Li, X., Using MODIS Land Surface Temperature and Normalized Difference Vegetation Index Products for Monitoring Drought in the Southern Great Plains, USA, International Journal of Remote Sensing; 25:61-72, 2004.

Wan, Z., New refinements and validation of the MODIS Land-Surface Temperature/Emissivity products, Remote Sensing of Environment 112 (2008):59–74.

Wang, K.; Wan, Z.; Wang, P.; Sparrow, M. ; Liu, J.; Zhou, X.; Haginoya, S. Estimation of surface long wave radiation and broadband emissivity using MODIS land surface temperature/emissivity product. J. Geophys. Res. 2005, 110, D11109.

Weng, Q. (2009). Thermal infrared remote sensing for urban climate and environmental studies: methods, applications, and trends. ISPRS Journal of Photogrammetry and Remote Sensing, 64, 335–344.

Weng, Q., Lu, D., & Schubring, J. (2004). Estimation of land surface temperature vegetation abundance relationship for urban heat island studies. Remote Sensing of Environment, 89, 467–483.

Yu, Y., Tarpley, D., Xu, H., GOES-R ABI ATBD for LST, http://www.goes-r.gov/products/ATBDs/baseline/baseline-LST-v2.0.pdf

Yu, Y., and I. J. Barton, A non-regression-coefficients method of sea surface temperature retrieval from space, Int. J. Rem. Sens., 15, 1189-1206, 1994.

Yu, Y., J. L. Privette, and A. C. Pinheiro, Analysis of the NPOESS VIIRS land surface temperature algorithm using MODIS data, IEEE Trans. Geosci. Remote Sens., vol. 43, no. 10, pp. 2340–2350, Oct. 2005.

Yu, Y., Ana C. Pinheiro, J L. Privette, Correcting land surface temperature measurements for directional emissivity over 3-D structured vegetation, SPIE San Diego , July, 2006.

Yu, Y., J. P. Privette, and A. C. Pinheiro, Evaluation of split window land surface temperature algorithms for generating climate data records, IEEE Trans. Geosci. Remote Sensing, vol. 46, No. 1, pp. 179-192, 2008.

Yu, Y., D. Tarpley, J. L. Privette, M. K. Rama Varna Raja, K. Vinnikov, H. Xu, Developing algorithm for operational GOES-R land surface temperature product, *IEEE Trans. Geosci. Remote Sens.*, *vol. 47*, no. 3, pp. 936-951, 2009a.

Yu. Y., J. L. Privette, Mitchell Goldberg, and D. Sun, Evaluation of the GOES land surface temperature algorithm using tower-based measurements from SURFRAD network, Proc., Second Conference on Earth Observation for Global Change, Chengdu, China, 2009b.

Yu. Y., M. Chen, K. Vinnikov, D. Tarpley, and H. Xu, A Three-measurement Model Developed for Evaluating Satellite Land Surface Temperature Product, SPIE 2009, San Diego, 2009c.

Yu. Y., H. Xu, D. Tarpley, and M. Goldberg, A Simplified method for measuring land surface temperature and emissivity using thermal infrared split-window channels, IGARSS 2009, Proc., Cape Town, 2009d.

Yu. Y., D. Tarpley, J. L. Privette, L. E. Flynn, H. Xu, M. Chen, K. Vinnikov, D. Sun, Y. Tian, Validation of GOES-R satellite land surface temperature algorithm using SURFRAD ground measurements and statistical estimates of error properties, *IEEE Trans. Geosci. Remote Sens.*, vol. 50, pp. 704-713, 2012.

Zheng, W.; Wei, H.; Wang, Z.; Zeng, X.; Meng, J.; Ek, M.; Mitchell, K.; Derber, J. Improvement of daytime land surface skin temperature over arid regions in the NCEP GFS model and its impact on satellite data assimilation. J. Geophys. Res.: Atmos. 2012, 117, D06117.

END OF DOCUMENT